

Gas dynamics and outflow in the barred starburst galaxy NGC 1808 revealed with ALMA

Dragan Salak

*Department of Physics, School of Science and Technology, Kwansai Gakuin University,
Gakuen 2-1 Sanda, Hyogo 669-1337, Japan*

d.salak@kwansai.ac.jp

Naomasa Nakai and Takuya Hatakeyama

*Division of Physics, Faculty of Pure and Applied Sciences, University of Tsukuba,
Tennodai 1-1-1, Tsukuba, Ibaraki 305-8571, Japan*

and

Yusuke Miyamoto

*Nobeyama Radio Observatory, National Astronomical Observatory of Japan, 462-2
Nobeyama, Minamimaki, Minamisaku, Nagano 384-1305, Japan*

ABSTRACT

NGC 1808 is a nearby barred starburst galaxy with an outflow from the nuclear region. To study the inflow and outflow processes related to star formation and dynamical evolution of the galaxy, we have carried out ^{12}CO ($J = 1 - 0$) mapping observations of the central $r \sim 4$ kpc of NGC 1808 using the Atacama Large Millimeter/submillimeter Array (ALMA). Four distinct components of molecular gas are revealed at high spatial resolution of $2''$ (~ 100 pc): (1) a compact ($r < 200$ pc) circumnuclear disk (CND), (2) $r \sim 500$ pc ring, (3) gas-rich galactic bar, and (4) spiral arms. Basic geometric and kinematic parameters are derived for the central 1-kpc region using tilted-ring modeling. The derived rotation curve reveals multiple mass components that include (1) a stellar bulge, (2) nuclear bar and molecular CND, and (3) unresolved massive ($\sim 10^7 M_{\odot}$) core. Two systemic velocities, 998 km s^{-1} for the CND and 964 km s^{-1} for the 500-pc ring, are revealed, indicating a kinematic offset. The pattern speed of the primary bar, derived by using a cloud-orbit model, is $56 \pm 11 \text{ km s}^{-1} \text{ kpc}^{-1}$. Non-circular motions are detected associated with a nuclear spiral pattern and outflow in the central 1-kpc region. The ratio of the mass outflow rate to the star formation rate is $\dot{M}_{\text{out}}/SFR \sim 0.2$ in the case of optically thin CO (1-0) emission in the outflow, suggesting low efficiency of star formation quenching.

Subject headings: galaxies: individual (NGC 1808) — galaxies: ISM — galaxies: kinematics and dynamics — galaxies: nuclei — galaxies: starburst — ISM: structure

1. Introduction

Inflows and outflows of baryons play important roles in galaxy evolution. In addition to circular rotation, observations of the interstellar medium (ISM) using molecular spectroscopy have revealed significant non-circular motions of gas clouds in galaxies. These motions are often observed in galaxies that exhibit non-axisymmetric gravitational potential due to spiral and bar structures, and in those that undergo tidal interaction with their neighbours. We consider the following four-step evolutionary process: (1) cold gas is transported toward the galactic center by gravitational torques, i.e., by losing angular momentum, or by accretion from intergalactic medium (IGM). One of the consequences of gas infall is the crowding of giant molecular clouds (GMCs) in nuclear rings at the outermost inner Lindblad resonance (radius a few 100 pc), resulting in (2) efficient feeding of star formation activity (e.g., Athanassoula 1992b; Buta & Combes 1996; Pérez-Ramírez et al. 2000). Bursts of star formation (starburst episodes), in turn, may trigger (3) outflows of ISM material (feedback) that remove molecular gas via supernova explosions and stellar winds, thereby suppressing further star formation in some regions while igniting it in others by outflow-induced shocks (e.g., Chevalier & Clegg 1985; Schiano 1985; Murray et al. 2005, 2011; Veilleux et al. 2005; Nath & Silk 2009; Bolatto et al. 2013a). Nuclear rings are also important gas reservoirs that may fuel the central accretion disks via nuclear (secondary) bars or spiral arms down to a scale of ~ 10 pc (e.g., García-Burillo et al. 2005; Combes et al. 2014), though the mechanism of angular momentum removal from kiloparsec to sub-parsec scale is not fully understood. Finally, the expelled ISM can either fall back onto the galaxy as a fountain, or escape and pollute the IGM with heavy elements, eventually (4) accreting onto another galaxy.

In order to study gas dynamics related to the inflow/outflow cycle in starburst galaxies and the evolution of GMCs in barred galactic disks, comprehensive observations are necessary. While GMC-scale studies require angular resolution ~ 100 pc or better, diffuse outflows can be detected only in measurements with high surface-brightness sensitivity. This is now readily achievable with the superb imaging capabilities of the Atacama Large Millimeter/submillimeter Array (ALMA) (e.g., Combes et al. 2013; García-Burillo et al. 2014; Sakamoto et al. 2014). In this work, we have used ALMA to image the molecular gas traced with the rotational line ^{12}CO ($J = 1 - 0$) in the nearby (10.8 Mpc; Tully 1988) starburst galaxy NGC 1808. As briefly described below, the galaxy is a promising case-study target

that shows signatures of the feeding/feedback evolution in the nearby Universe.

NGC 1808 is a (R)SAB(s)a barred spiral galaxy (de Vaucouleurs et al. 1991) known for peculiar “hot spots” in the star-forming central 500-pc region (Morgan 1958; Sérsic & Pastoriza 1965), and prominent polar dust lanes (figure 1) revealed in optical studies (Burbidge & Burbidge 1968; Phillips 1993) that indicate an outflow of dust and neutral gas. The central region is dotted with radio and infrared sources revealing supernova remnants and young star clusters (Saikia et al. 1990; Forbes et al. 1992; Krabbe et al. 1994; Kotilainen et al. 1996; Tacconi-Garman et al. 1996; Galliano & Alloin 2008), while the galactic center harbors a candidate for a low-luminosity active galactic nucleus (AGN) (Véron-Cetty & Véron 1985; Awaki et al. 1996; Jiménez-Bailón et al. 2005). Atomic gas traced with the HI 21-cm line is concentrated in the galactic bar, disk, and a warped outer ring, indicating a tidal interaction in the past (Koribalski et al. 1993, 1996). The galaxy has been observed in CO before, although only with single-dish telescopes at low angular resolution of $\gtrsim 22''$ (Dahlem et al. 1990; Aalto et al. 1994; Salak et al. 2014). In this work, we present the first high-resolution CO (1-0) and 2.8-mm band continuum data.

The paper is organized as follows. In section 2, we describe the observations and data reduction. The results are presented in section 3, including the properties of the continuum and CO (1-0) line emission on the galaxy scale, followed by discussion (sections 4, 5, and 6) where we focus on the central 1-kpc molecular zone (CO gas distribution, kinematics, and dynamics) and briefly address the dynamics of the large-scale bar. A dynamical model is introduced in section 4, extended by an analysis of the molecular gas outflow in section 5. Finally, star formation is briefly discussed in section 6. Analyses of the galaxy-scale GMC properties and star formation in the bar are the subject of a forthcoming paper that includes combined 12-m array, 7-m array (ACA), and total power data (Salak et al. in prep.). The work is summarized in the last section.

The basic parameters of NGC 1808 are listed in table 1. The velocity in this paper is defined with respect to the local standard of rest (LSR) in radio definition, and all images are displayed in equatorial coordinates $(\alpha, \delta)_{J2000.0}$.

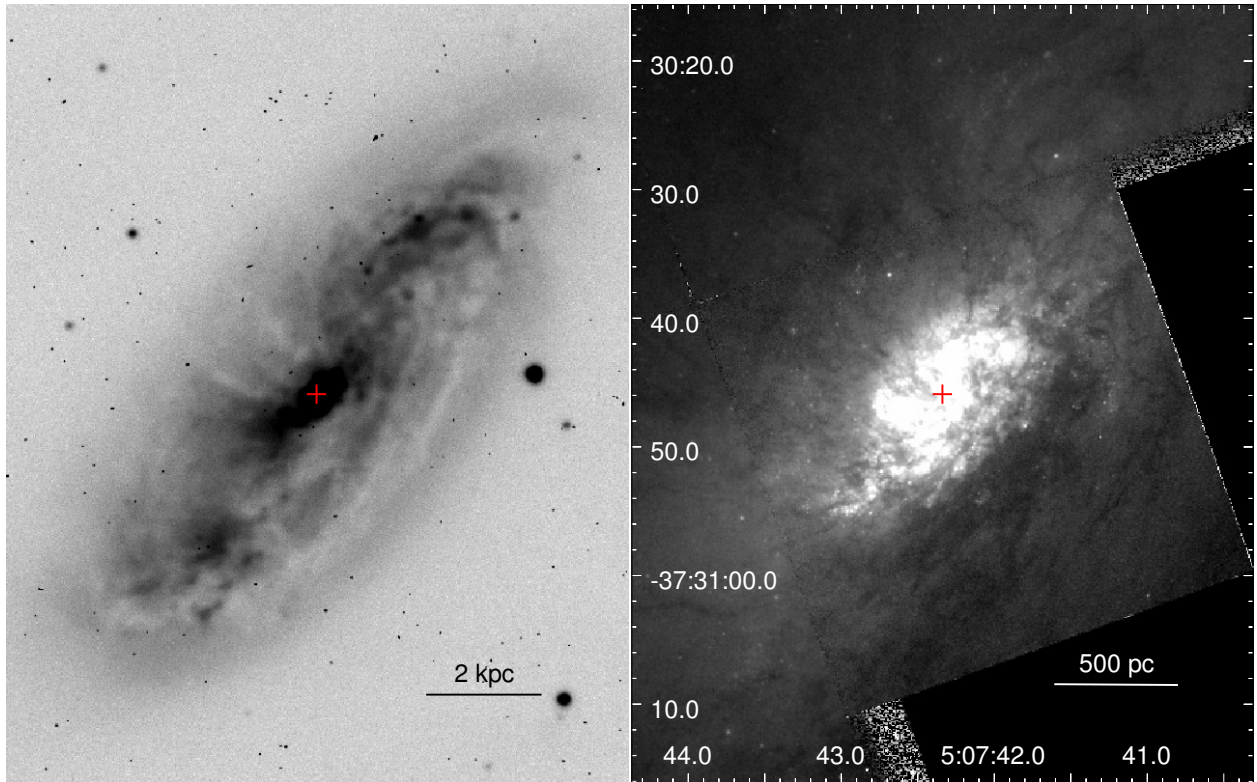


Fig. 1.— *Left.* Large-scale R -band negative image of NGC 1808 (Meurer et al. 2002). The cross marks the galactic center determined from our continuum observations (section 3.1). Dust lanes perpendicular to the galactic disk suggest outflows. *Right.* HST image (675W) of the central region (acquired from Hubble Legacy Archive).

Table 1: Basic parameters of NGC 1808.

Right ascension (J2000.0) ^a	05 ^h 07 ^m 42 ^s .343
Declination (J2000.0) ^a	−37°30′45″.95
Distance ^b	10.8 Mpc
Adopted linear scale	1″ = 52 pc
Systemic velocity (LSR) ^c	963.9 ± 2.5 km s ^{−1} (global)
	998.4 ± 2.5 km s ^{−1} ($r < 235$ pc)
Position angle ^d	324°
Inclination ^e	57°
Morphological type ^f	(R)SAB(s)a
Activity ^g	HII, Seyfert 2 (?)

^aDerived in this work from the peak of the 2.8-mm continuum emission (see table 3).

^bTully (1988).

^cDerived in this paper from the CO (1-0) line profile.

^dDerived in this work for the central 1 kpc from CO kinematics and a K_s -band image; receding side of the galaxy measured from N toward E. The derived value is close to the global one found in optical studies (323°; Lauberts & Valentijn 1989).

^eReif et al. (1982).

^fde Vaucouleurs et al. (1991).

^gNED classification.

2. Observations and data reduction

Observations were conducted on 2014 March 8, with twenty seven antennas of the ALMA 12-m array as part of our cycle 1 project. The imaging was performed toward 39 fields combined into a $150'' \times 150''$ mosaic (about 7.5×7.5 kpc² at the adopted distance of 10.8 Mpc) shown in figure 2. The shortest projected baseline of the 12-m array was $L_{\min} \approx 15$ m, hence the visibilities that correspond to $(u, v) \lesssim 6$ k λ , where λ is the observed wavelength, were not sampled (see figure 3). The maximum recoverable scale per pointing is $\theta_{\text{MRS}} \simeq 0.6\lambda/L_{\min} \approx 21''$; any structure larger than this is entirely filtered out. The longest baseline of the 12-m array was $L_{\max} = 423$ m, allowing sampling of high spatial frequencies (angular resolution given by $\theta = k\lambda/L_{\max}$, where k is a constant that depends on the weighting function). The cycle 1 project includes supplement observations using the Atacama Compact Array (ACA) and total power (TP) arrays needed to recover extended emission and total flux, and the combined data will be presented in a future paper. The sources used as calibrators were: Callisto (flux density), J0609-1542 (bandpass), and J0522-3627 (phase). The total on-source time was about 41 minutes, but the integration time per pointing was about 1 minute. Four spectral windows at the rest frequencies of (1) 101.271, (2) 103.200, (3) 113.271, and (4) 115.271202 GHz (rest frequency of the rotational transition CO 1-0) were observed simultaneously, each with a bandwidth of 2 GHz except window 4 which had a bandwidth of 1.870 GHz (4892.3 km s⁻¹) and high spectral resolution of 976.56 kHz (2.548 km s⁻¹) to resolve the CO (1-0) line.

Data reduction was carried out using the Common Astronomy Software Applications (CASA) package (McMullin et al. 2007). The data were calibrated, continuum-subtracted, deconvolved using the CLEAN algorithm with Briggs weighting. The CLEAN procedure was carried out interactively until the residual map resembled pure noise. The iteration was then proceeded automatically until a threshold of about 1σ was reached. This threshold was adopted by inspecting emission-free channels in the dirty map. As a result, despite a relatively coarse (u, v) coverage, side lobes were successfully suppressed to negligible levels comparable to 1σ r.m.s. Two images were produced to analyze different galactic scales: (1) high-resolution image with robust = 0.5, velocity resolution of 2.548 km s⁻¹, and spatial resolution [the full-width at half maximum (FWHM) of the synthesized beam] of $2''.26 \times 1''.23$ (117 pc \times 64 pc) for the galactic central region where the signal-to-noise ratio is highest, and (2) high-sensitivity image with robust = 2 and velocity resolution 10.192 km s⁻¹ to increase the sensitivity of extended structure over the entire mosaic. The angular resolution in the final data cube (robust = 2) is $2''.55 \times 1''.41$ (133 pc \times 73 pc). The r.m.s. sensitivity of the CO image in emission-free channels is 5.5 mJy beam⁻¹ per velocity bin of 10.2 km s⁻¹, or about 0.14 K (1σ) in brightness temperature units. The final continuum image produced by multi-frequency synthesis using four spectral windows after subtracting the contribution

from CO (1-0) has a sensitivity of $0.20 \text{ mJy beam}^{-1}$. The continuum image was created with $\text{robust} = 0.5$ weighting to achieve a compromise between angular resolution and sensitivity expecting that emission is confined to the galactic nuclear region. The images presented in figures are not corrected for primary beam attenuation, except those of the central region. The images were corrected, however, in order to derive fluxes and masses.

Observational parameters are summarized in table 2.

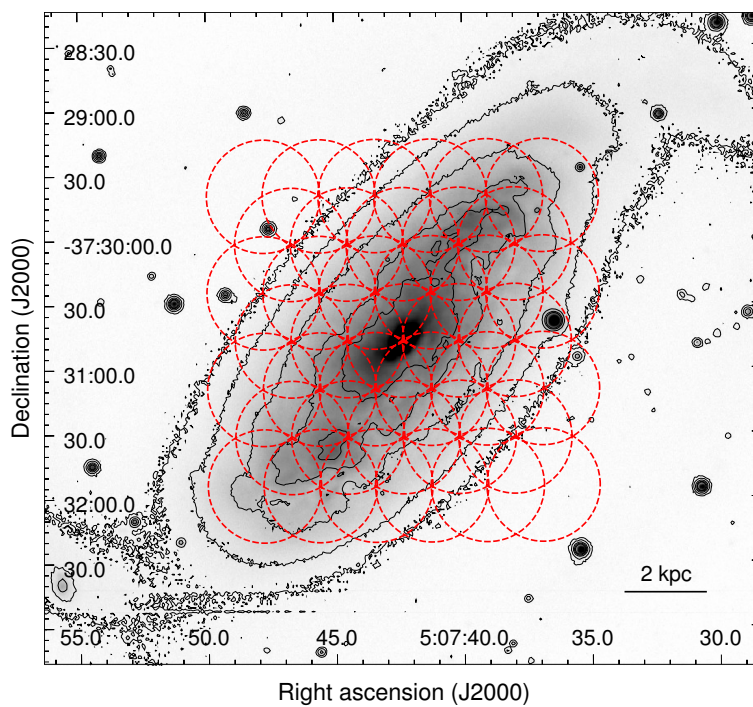


Fig. 2.— Observed fields (39 pointings) superimposed on an *R*-band negative image of NGC 1808 (same as in figure 1); the circle size is the primary beam with a FWHM of $52''$ (approx. $1.13\lambda/D$ where $D = 12$ m). Contours are plotted on a square root scale from 0.1% to 2% of the peak intensity.

Table 2: Observational summary.

ALMA 12-m array	
Number of antennas	27
Observation date	2014 March 8
Flux calibrator	Callisto
Bandpass calibrator	J0609-1542
Phase calibrator	J10522-3627
Map size	$150'' \times 150''$ (7.8×7.8 kpc ²)
Mosaic	39 fields (Nyquist sampling)
Primary beam FWHM ($\lambda = 2.7$ mm)	$52''$
Synthesized beam	$\theta_{\text{maj}} \times \theta_{\text{min}}$
High sensitivity, FWHM ^a	$2''.55 \times 1''.41$
High resolution, FWHM ^b	$2''.26 \times 1''.23$
Total time on source	41 min
Sensitivity	1σ
High sensitivity, CO (1-0) ^a	$5.5 \text{ mJy beam}^{-1}$
High resolution, CO (1-0) ^b	$10.0 \text{ mJy beam}^{-1}$
Continuum ^c	$0.20 \text{ mJy beam}^{-1}$

^aBriggs weighting with robust = 2 and velocity resolution $\Delta v = 10.2 \text{ km s}^{-1}$.

^bBriggs weighting with robust = 0.5 and velocity resolution $\Delta v = 2.5 \text{ km s}^{-1}$.

^cBandwidth per spectral window $B = 2 \text{ GHz}$.

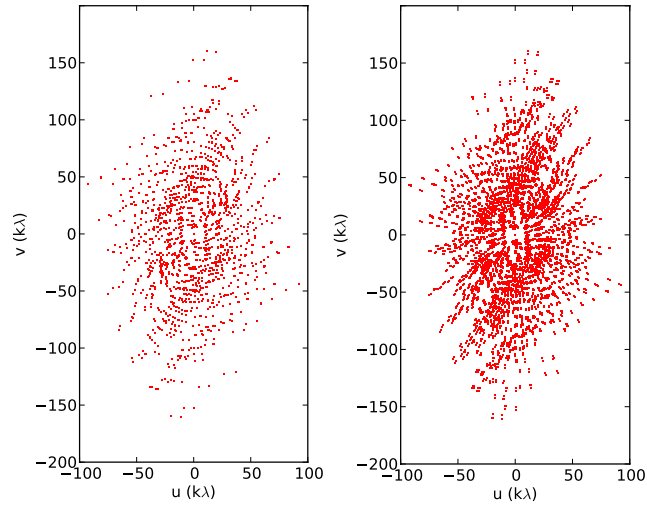


Fig. 3.— (u, v) coverage of the central pointing of the CO (1-0) observation (left), and continuum observation (right).

3. Results

3.1. Continuum emission

Radio continuum in NGC 1808 was previously observed at low frequencies (20, 6, 3.6, and 2 cm) that revealed several “hot spots” in the galactic central region (e.g., Condon 1987; Saikia et al. 1990; Collison et al. 1994; Kotilainen et al. 1996). Our simultaneous observations of four spectral windows (sub-bands with frequencies between 100 and 115 GHz) yielded wide-field, sensitive, high-resolution continuum images that add new information about the complex starburst region (figure 4). In total, six sources were detected within $r < 400$ pc from the galactic center with a significance of $> 3 \sigma$ and three sources with $> 5 \sigma$ including the nucleus (13σ) and two circumnuclear hot spots. The circumnuclear sources are denoted by C1-C5 in figure 4. The locations and flux densities of all sources are derived by 2-dimensional Gaussian fitting and the results are presented in tables 3 and 4. Some of the sources are unresolved as their shapes resemble the synthesized beam, but the nucleus appears slightly extended toward east and north-east, as well as the elongated source C4 south-east of the nucleus. The emission peak is located at $(\alpha, \delta)_{J2000.0} = (5^{\text{h}}7^{\text{m}}42^{\text{s}}.343, -37^{\circ}30'45''.95)$.

The flux density S_ν of the continuum emission can be expressed as a function of frequency ν , $S_\nu \propto \nu^\alpha$, where α is the spectral index. Depending on the mechanism that generates the continuum emission at the observed frequency, the spectral index can vary from negative to positive values (e.g., Condon 1992). At 2.8 mm, we expect a combination of free-free emission (nearly flat frequency dependence), blackbody emission from dust grains (positive α), and non-thermal synchrotron emission from accelerated electrons in magnetic fields (negative α). To investigate the nature of the continuum emission in the nuclear region, we derived a spectral index distribution from two images, each produced by a synthesis of two spectral windows: the upper-frequency image was produced from spectral windows 3 and 4 (113 and 115 GHz), denoted ν_u , while the lower-frequency image was produced from spectral windows 1 and 2 (101 and 103 GHz), denoted ν_l . The spectral index, as the slope of the spectrum between the two frequency sets, is defined by

$$\alpha(\nu) \equiv \frac{\log(S_u/S_l)}{\log(\nu_u/\nu_l)}, \quad (1)$$

and the resulting α image is shown in figure 5. In the central $r < 100$ pc, the spectral index varies in the range $-3 \lesssim \alpha \lesssim 1$ with $\alpha_{\text{core}} \simeq -1$ at the galactic center position. These values indicate mixed free-free radiation in hot ionized gas, where α is typically close to 0 in optically thin HII regions, and non-thermal synchrotron radiation from fast electrons accelerated in, e.g., supernova remnants. In addition to free-free emission, flattening of a non-thermal radiation spectrum can occur due to self-absorption of synchrotron radiation.

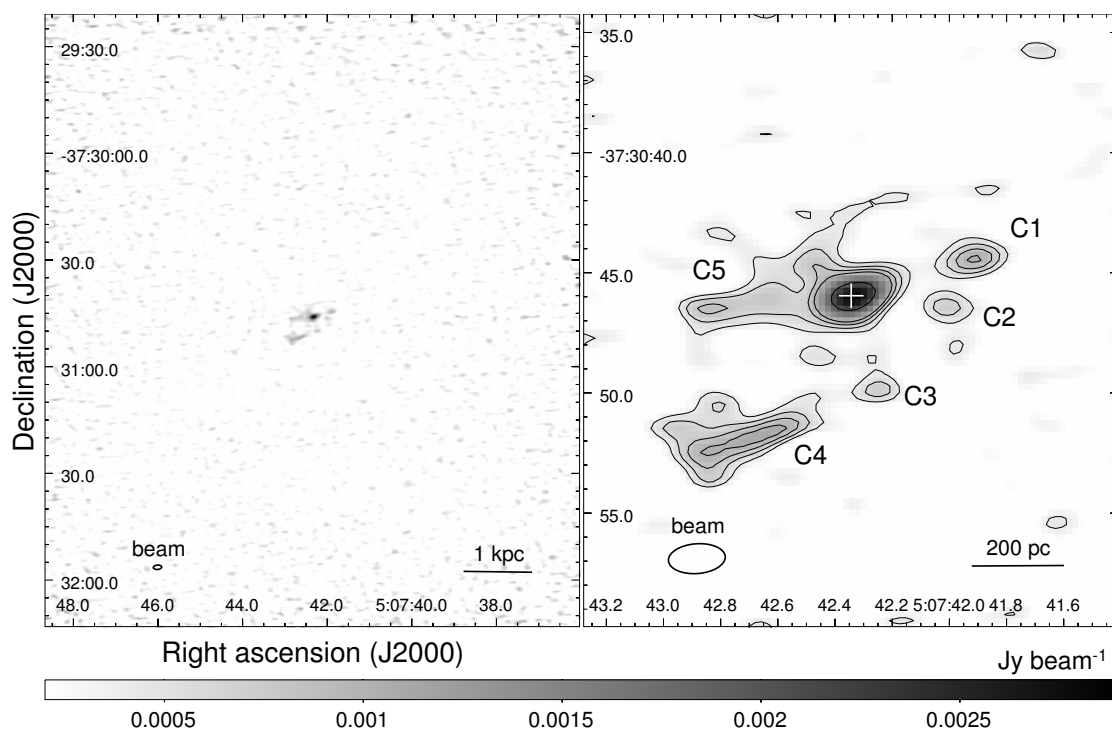


Fig. 4.— Continuum emission synthesized from emission-free channels of four spectral windows: total image (left) and the central 1 kpc (right). The color is shown on a linear scale starting from $0.3 \text{ mJy beam}^{-1}$ (1.5σ) with contours at 0.4, 0.6, 0.8, 1, 2 mJy beam^{-1} . The cross marks the galactic center determined from Gaussian fitting (see table 3). The synthesized beam is shown at the bottom left corner.

Table 3: Properties of the central continuum source derived from 2-dimensional Gaussian fitting.

Peak position α_{J2000}	$05^{\text{h}}07^{\text{m}}42^{\text{s}}.3434 \pm 0.0097$
Peak position δ_{J2000}	$-37^{\circ}30'45''.955 \pm 0.059$
Major axis (FWHM) ^a	$1''.67 \pm 0''.49$ (87 ± 25 pc)
Minor axis (FWHM) ^a	$1''.22 \pm 0''.77$ (63 ± 40 pc)
Position angle ^a	$130^{\circ} \pm 52^{\circ}$
Total flux density	4.68 ± 0.57 mJy
Peak flux density	2.64 ± 0.22 mJy beam ⁻¹

^aDeconvolved from a clean beam with size (FWHM) $2''.37 \times 1''.24$ and position angle $PA = -85^{\circ}.74$ at reference frequency $\nu_{\text{ref}} = 107.8849$ GHz. The fitting region is a circle of diameter $4''$ centered on the flux density peak of the convolved image.

Table 4: Properties of circumnuclear continuum sources detected with $> 3\sigma$ derived from 2-dimensional Gaussian fitting.

Source	α_{J2000}	δ_{J2000}	Peak intensity [mJy beam ⁻¹]	Detection significance [σ]
C1	$05^{\text{h}}07^{\text{m}}41^{\text{s}}.92$	$-37^{\circ}30'44''.41$	1.024 ± 0.050	5.1
C2	$05^{\text{h}}07^{\text{m}}42^{\text{s}}.01$	$-37^{\circ}30'46''.43$	0.680 ± 0.041	3.4
C3	$05^{\text{h}}07^{\text{m}}42^{\text{s}}.25$	$-37^{\circ}30'49''.77$	0.716 ± 0.060	3.6
C4	$05^{\text{h}}07^{\text{m}}42^{\text{s}}.71$	$-37^{\circ}30'51''.93$	1.114 ± 0.054	5.6
C5	$05^{\text{h}}07^{\text{m}}42^{\text{s}}.82$	$-37^{\circ}30'46''.59$	0.856 ± 0.078	4.3

The derived spectral index is similar to that of $\alpha_{\text{core}} = -0.9$ found by Dahlem et al. (1990) by comparing 20 and 6 cm images. By contrast, the compact sources that surround the nucleus on average exhibit $\alpha \gtrsim 0$. Such values of α can be produced in thermally-cooling regions with free-free and dust-grain emission. In fact, the compact sources except the core are not detected at the lower frequency, resulting in lower limits. The spectral index in these obscured regions may also be affected by optical depth and other variations in dust properties.

From the derived values of α , we suggest that the nucleus is dominated by a high-energy source, e.g., nuclear starburst accompanied with supernova explosions and/or a low-luminosity AGN [indicated from optical and X-ray studies too, e.g., Véron-Cetty & Véron (1985), Awaki et al. (1996), and Jiménez-Bailón et al. (2005)], confirming the results from previous radio-continuum observations (e.g., Collison et al. 1994). The circumnuclear sources may be compact HII regions, possibly associated with young star clusters embedded in dusty clouds detected at infrared wavelengths (Galliano & Alloin 2008).

In figure 6 we show a comparison of our 2.8-mm continuum data with 3.6-cm continuum sources and the most luminous nuclear X-ray sources at 0.3-0.9 keV (S1) and at 2-10 keV (S2). The spectral indices of low-frequency sources indicate that their nature is supernova remnants (Saikia et al. 1990; Collison et al. 1994). However, the 2.8-mm sources revealed in ALMA images are only partially coincident with these objects, suggesting that the 2.8-mm and 3.6-cm sources are not identical in most cases.

As for the X-ray data, S1 is obscured by a hydrogen column density of $N_{\text{H}} \sim 0.6 \times 10^{22} \text{ cm}^{-2}$ and harbors a source with luminosity $L_{\text{X}} \sim 1.5 \times 10^{39} \text{ erg s}^{-1}$ in the 2-10 keV band (Jiménez-Bailón et al. 2005; Heike & Awaki 2007), somewhat lower than the low-luminosity AGN in nearby galaxies $[(0.4-50) \times 10^{40} \text{ erg s}^{-1}$; Terashima et al. 2002]. Although both sources emit radiation in the hard X-ray band (S2 being more luminous with $L_{\text{X}} \sim 9.2 \times 10^{39} \text{ erg s}^{-1}$), only source S1 has a counterpart at 2.8 mm and longer wavelengths.

The distribution of radio sources around the nucleus (figure 6) indicates the presence of a partial ionized gas ring (radius $r_{\text{ion}} \simeq 7.5''$ or 390 pc), inclination $i \simeq 60^\circ$, and position angle $PA \simeq 310^\circ$, consistent with the global parameters of the galaxy (derived in section 4). As we show below, the ionized gas ring lies on the inner edge of a pseudo-ring of molecular gas detected in CO (1-0), and it is this inner region where most of the star-forming activity and its feedback (supernova explosions) is taking place. Since our data were taken over a wide mosaic field, imaging was not restricted by the field of view (except the lack of short-spacing baselines); no 2.8-mm continuum emission is detected beyond the ionized ring.

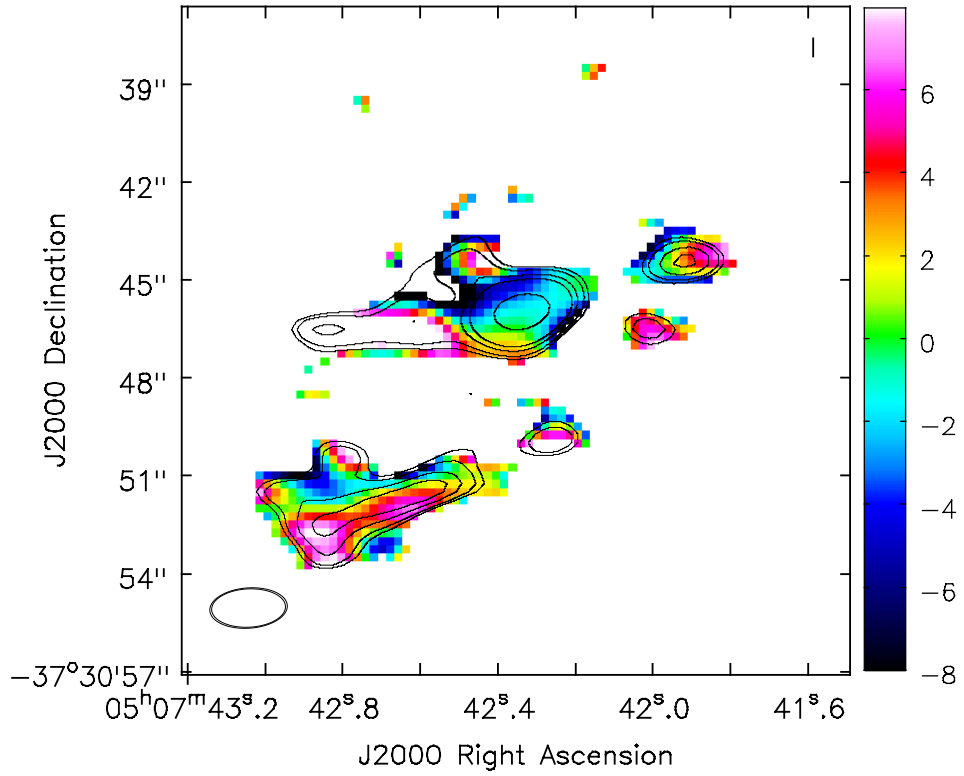


Fig. 5.— Spectral index distribution calculated from synthesized images of the upper sub-bands at 113 and 115 GHz (ν_u) and the lower sub-bands at 101 and 103 GHz (ν_l). The contours are the same as in figure 4.

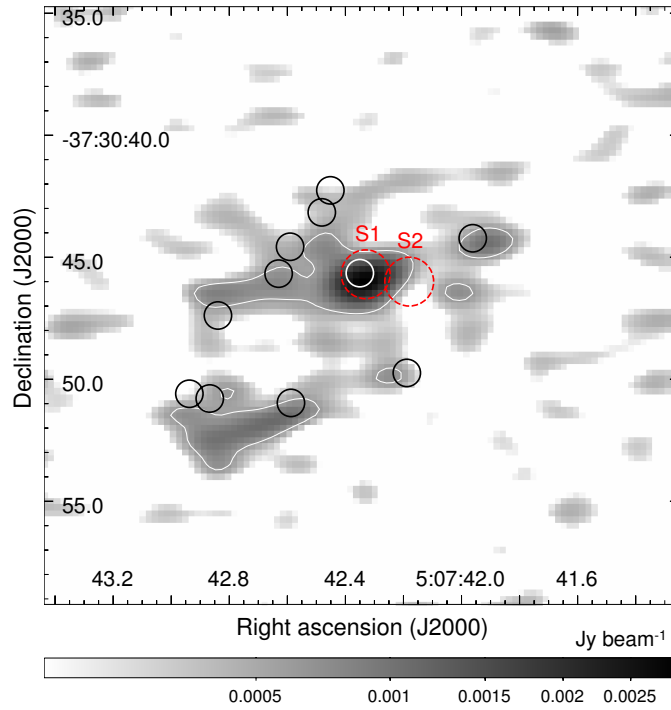


Fig. 6.— Compact 3.6-cm sources (full circles) from Collison et al. (1994) and luminous X-ray sources (dashed circles S1 and S2) from Jiménez-Bailón et al. (2005) and Heike & Awaki (2007) superimposed on our 2.8-mm continuum image (grey scale). S1 is the location of the obscured low-luminosity AGN candidate. The contour is plotted at 3σ .

3.2. Molecular gas distribution

In this section we present the first high-resolution interferometric observations of CO in NGC 1808. Molecular gas traced by CO (1-0) emission is detected throughout the galactic disk (moment 0 defined as $I_{\text{CO}} \equiv M_0 = \Delta v \sum \mathcal{S}_i$, where $\Delta v = 10.2 \text{ km s}^{-1}$ and \mathcal{S}_i is the CO (1-0) flux density per beam, shown in figure 7a), with four distinct regions: (1) compact circumnuclear disk (CND) or torus confined to $r < 200 \text{ pc}$ (peak emission $I_{\text{CO}}^{\text{max}} = 41 \text{ Jy beam}^{-1} \text{ km s}^{-1}$ in the high-sensitivity image), (2) pseudo-ring¹ at 500 pc from the center, (3) giant molecular clouds (GMCs) and associations (GMAs) in the large-scale bar, and (4) GMCs in the disk where compact CO (1-0) emission is detected predominantly in spiral arms. An illustration of the main structures of molecular gas is shown in figure 7. The sensitivity of the CO (1-0) image ($5.5 \text{ mJy beam}^{-1}$) is equivalent to $\sim 7 \times 10^4 M_{\odot}$, where the luminosity-to-mass conversion was done using a Galactic CO-to-H₂ conversion factor of $X_{\text{MW}} = 2 \times 10^{20} \text{ cm}^{-1} (\text{K km s}^{-1})^{-1}$ (Bolatto et al. 2013b). The resolution and sensitivity are sufficient to detect typical Galactic GMCs ($4 \times 10^5 M_{\odot}$; Young & Scoville 1991) in the disk with 5σ significance. A comparison with a 2MASS (Two-Micron All Sky Survey; Jarrett et al. 2003) image in K_s -band tracing old and middle-aged stellar populations (figure 7b) shows that molecular gas is concentrated in the bulge region and the leading side of the large-scale bar (figure 7c). In the central starburst zone, CO is detected in the region between the 500-pc ring and the CND in a nuclear disk with complex morphology and kinematics. We begin by describing the details of the large-scale morphology.

3.2.1. Large-scale bar and spiral arms

Outside the central starburst region, molecular gas is concentrated in a bar (semi-major axis $a_b \simeq 3 \text{ kpc}$ estimated from the K_s -band image; figure 7b) and global spiral arm pattern (illustrated in figure 7c). The position angle of the bar is $PA_{\text{bar}} \simeq 335^\circ$, about 10° higher than the position angle of the galactic disk.

The most prominent feature of CO (1-0) emission in the bar is the concentration of molecular clouds along the “offset ridges” spatially correlated with the dust lanes on the leading side of the bar. These structures have been observed in numerous barred galaxies and have been reproduced by numerical and analytical calculations including the cloud orbit and hydrodynamical shock-wave models (e.g., Contopoulos 1980; Binney et al. 1991; Athanassoula 1992a,b; Lindblad & Lindblad 1994; Wada 1994; Sakamoto et al. 1999; Sheth et

¹The ring is part of a two-arm spiral pattern hence “pseudo”.

al. 2000; Hirota et al. 2014; and others). In the cloud orbit model, the lanes are a consequence of oval orbits of gas clouds in the bar potential. Upon crossing the bar region, the clouds orbiting in the galactic disk gain inward motion as seen from the rotating frame. Orbit crowding leads to increased gas concentration manifested in stronger CO (1-0) emission and dust extinction.

At other wavelengths, the bar is also rich in HI gas and dotted with HII regions revealed in H α (Koribalski et al. 1996). Enhanced intensity of the higher CO transition $J = 3 \rightarrow 2$ was also detected along the bar using the single-dish telescope ASTE (Salak et al. 2014).

In figures 8 and 9, we show a large-scale comparison of CO (1-0) observed by ALMA and a high-resolution HST image of H α . Outside the luminous starburst nucleus, we find that the bar harbors a number of large concentrations of molecular gas spatially correlated with H α . Consider, for example, a clump of CO gas marked with arrow in figure 9 (S panel). The integrated intensity enclosed within $r < 10''$ from the CO emission peak of this cloud is $I_{\text{CO}} = 46 \text{ Jy km s}^{-1}$. Using a CO-to-H $_2$ conversion formula (with a Galactic conversion factor), introduced in the next section, this yields a mass of $M_{\text{mol}} \approx 6 \times 10^7 M_{\odot}$. The object is a giant molecular association (GMA), and the comparison with H α shows that it is a site of star formation inside the bar. Similar masses can be derived for the GMAs in the north too, where HII regions are located in nearly a straight line aligned with the major axis of the bar. This behavior has been reproduced in recent numerical simulations where molecular clouds in bars form star-forming GMAs through merging and collisions (Fujimoto et al. 2014).

Outside the bar, individual GMCs can be identified in the disk, many of which are concentrated in structures that resemble a spiral pattern (figure 7c). In particular, several arms are connected to the bar and emerge from its ends, with notable asymmetry in the density of GMCs and HII regions: there are more molecular clouds and star-forming regions on the trailing side of the bar, especially around the NW semi-major axis. We leave a more quantitative analysis of the relation between CO and star-forming tracers to a future work that includes the short-spacing correction.

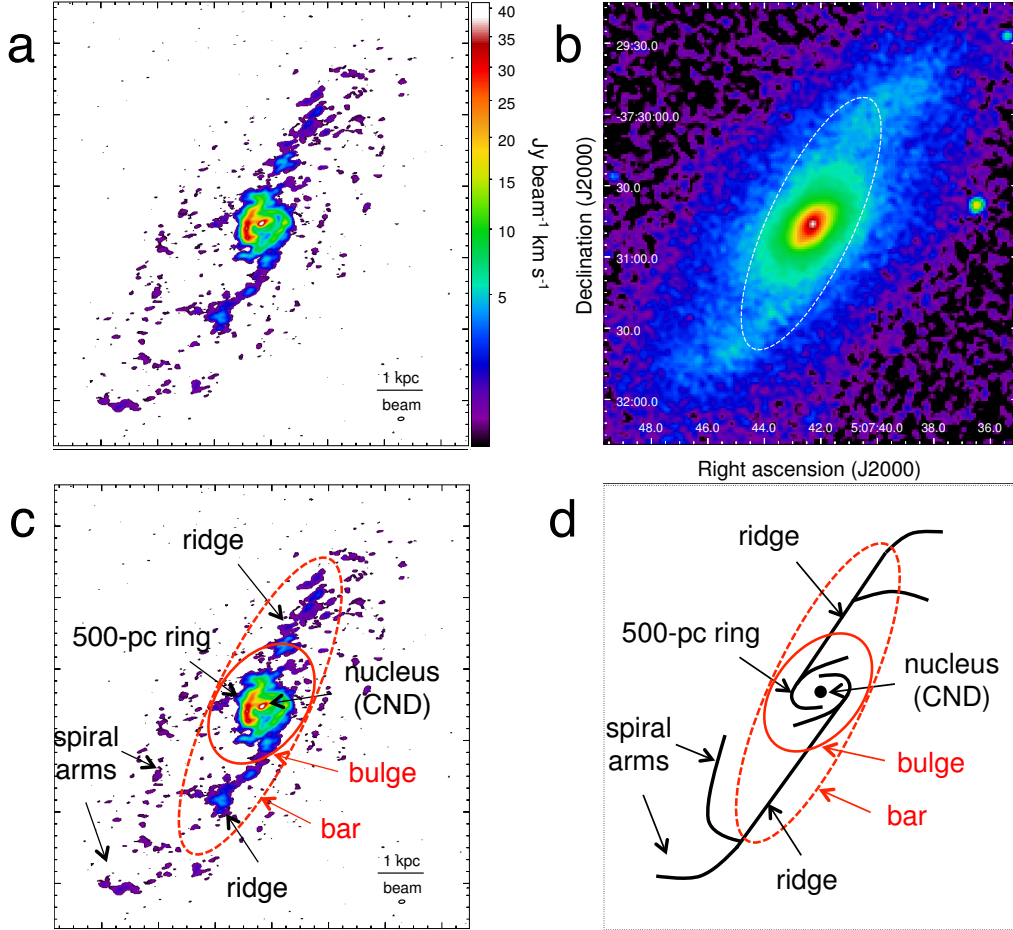


Fig. 7.— (a) High-sensitivity image of CO (1-0) integrated intensity (moment 0) presented on a square root scale from $0.22 \text{ Jy beam}^{-1} \text{ km s}^{-1}$ (pixels below 4σ , where $1\sigma = 5.5 \text{ mJy beam}^{-1}$, were masked) to the peak value of $41 \text{ Jy beam}^{-1} \text{ km s}^{-1}$. The synthesized beam ($2''.55 \times 1''.41$ at $PA = -82^\circ$) is shown at the lower right corner. (b) 2MASS image in K_s -band presented on a logarithmic scale (Jarrett et al. 2003). The bar region is indicated with a dashed ellipse (semi-major axis $a_b = 3 \text{ kpc}$). (c)-(d) Illustration of the galactic structure: the bulge and bar are shown in red, and the major molecular-gas components (nucleus, 500-pc ring, ridge, and spiral arms) in black color.

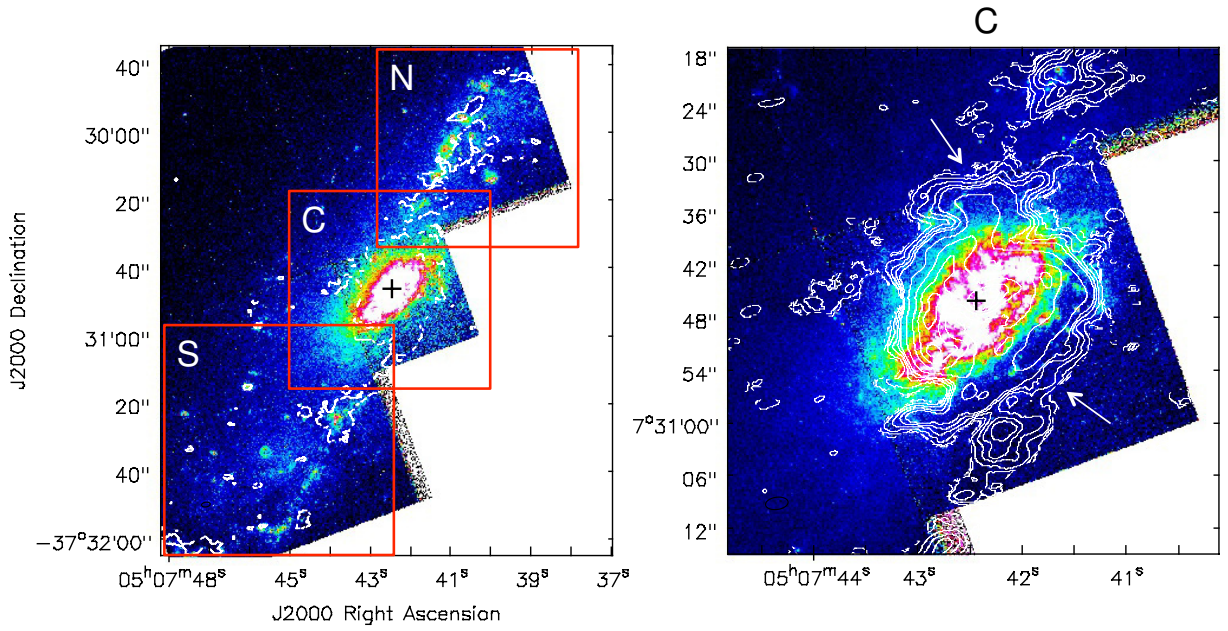


Fig. 8.— *Left.* H α emission in NGC 1808 (Hubble Legacy Archive) shown in color. The contour is CO (1-0) intensity at 1% of the peak $41 \text{ Jy beam}^{-1} \text{ km s}^{-1}$. The rectangles mark the regions shown in greater detail in panel on the right and in figure 9. *Right.* Enlargement of the central region C. The contours are plotted at 0.005, 0.01, 0.025, 0.05, 0.075, 0.1, 0.2, 0.4, 0.6, 0.8 times the peak. The white arrows mark the regions where the ridges of the bar connect to the 500-pc ring.

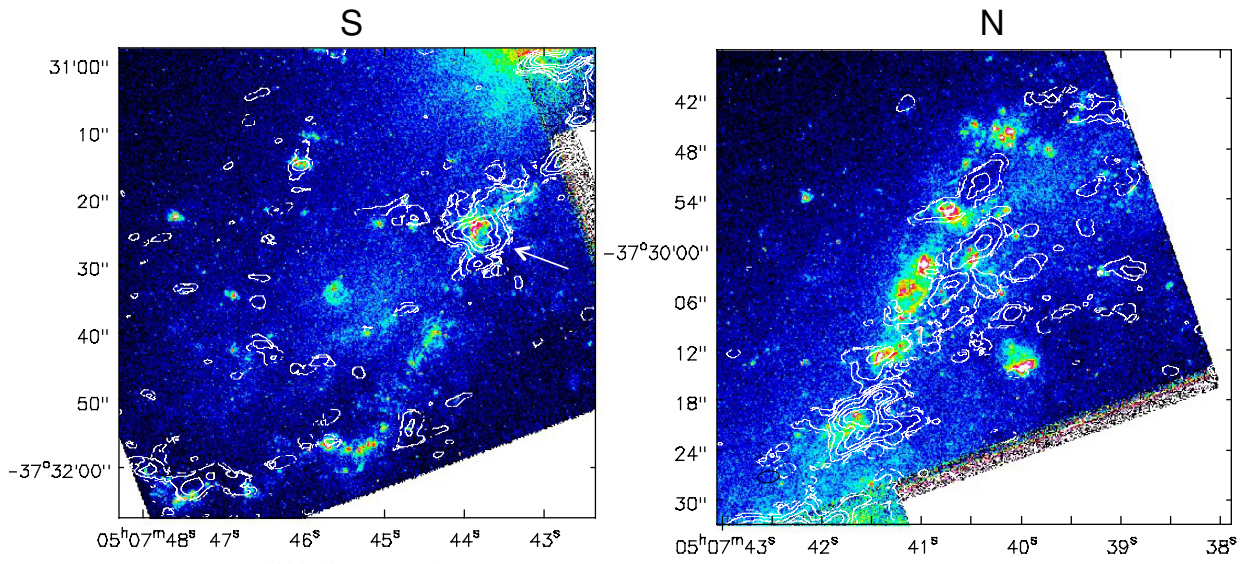


Fig. 9.— Regions S (south) and N (north) from figure 8, with the same contours. The white arrow marks the location of a GMA with an associated giant HII region (see text). Similar massive molecular complexes with star-forming regions are detected in the north too.

3.2.2. Gas surface density in the central starburst region

The CO (1-0) emission is prominent in the central $r \lesssim 800$ pc (figures 10 and 11). Emission peaks in the CND ($I_{\text{CO}} = 34 \text{ Jy beam}^{-1} \text{ km s}^{-1}$ in the high-resolution image) and in a 500-pc pseudo-ring that is part of a two-arm spiral. Molecular gas is also present between the center and the ring, where infrared observations reveal an embedded nuclear stellar bar at a position angle of $\simeq 335^\circ$ (Kotilainen et al. 1996; Tacconi-Garman et al. 2005). Note that the nuclear bar is well aligned with the large-scale bar. This is not a usual configuration as the bars in double-barred galaxies show random relative position angles, while different angular velocities of the two bars are produced in simulations (Heller et al. 2007). In the dynamical evolution, the nuclear bar is expected to change its pattern speed (e.g., accelerate its rotation during an alignment event) and possibly oscillate in thickness and ellipticity as the two bars constantly change the position angle with respect to each other (Debattista & Shen 2007; Maciejewski & Small 2010). Interestingly, there is no clear spatial correlation between the nuclear bar and the molecular gas distribution traced by CO: molecular gas is not following the bar with prominent ridges (as it is on the kiloparsec scale), but instead a nuclear spiral pattern indicated in figure 10. The spiral arm can be seen west and south-west of the nucleus at a radius of $r \sim 200$ pc ($3.8''$); it is spatially correlated with a dust lane visible as extinction on the HST image.

The mass of molecular gas in the central region can be calculated from $M_{\text{mol}} = 1.05 \times 10^4 (X_{\text{CO}}/X_{\text{MW}}) d^2 S_{\text{CO}} \Delta v [M_\odot]$, where X_{CO} is the CO-to- H_2 conversion factor, d distance to the galaxy in Mpc, S_{CO} measured flux density in Jy, and Δv velocity width (e.g., Bolatto et al. 2013b). Adopting a low conversion factor of $X = 0.8 \times 10^{20} \text{ cm}^{-2} (\text{K km s}^{-1})^{-1}$, estimated by Salak et al. (2014) for the central 1-kpc region of this galaxy using a radiative transfer analysis (kinetic temperature $T_k = 35$ K and gas density $n_{\text{H}_2} = 10^{3.5} \text{ cm}^{-3}$), $d = 10.8$ Mpc, and measured $S_{\text{CO}} \Delta v = 281 \text{ Jy km s}^{-1}$, we find a molecular gas mass (including He) of $M_{\text{mol}}(r < 250 \text{ pc}) \simeq 1.4 \times 10^8 M_\odot$ in the CND region. With a standard Galactic conversion factor of $2 \times 10^{20} \text{ cm}^{-2} \text{K}^{-1} (\text{km s}^{-1})^{-1}$, the mass is $3.4 \times 10^8 M_\odot$. This is about 23% of the total molecular gas mass in the central $r < 780$ pc detected with the 12-m array. The total CO (1-0) flux detected over the $150'' \times 150''$ mosaic image is $1521 \text{ Jy km s}^{-1}$ (corrected for primary beam attenuation) corresponding to $1.9 \times 10^9 M_\odot$. This is comparable to the total atomic gas mass ($M_{\text{HI}} = 1.7 \times 10^9 M_\odot$) over the central $\sim 4'$ estimated by Koribalski et al. (1993) from their large-field HI maps. All flux values are lower limits because short-spacing correction has not been applied. The masses are summarised in table 5.

The surface density of the H_2 gas when viewed face-on can be expressed as

$$\left(\frac{\Sigma_{\text{H}_2}}{M_\odot \text{ pc}^{-2}}\right) = 3.3 \times 10^2 \cos i \left(\frac{\Omega_{\text{A}}}{\text{arcsec}^2}\right)^{-1} \left(\frac{I_{\text{CO}}}{\text{Jy beam}^{-1} \text{ km s}^{-1}}\right) \left[\frac{X_{\text{CO}}}{2 \times 10^{20} \text{ cm}^{-2} (\text{K km s}^{-1})^{-1}}\right], \quad (2)$$

where Ω_{A} is the beam solid angle calculated as

$$\Omega_{\text{A}} = \frac{\pi \theta_{\text{maj}} \theta_{\text{min}}}{4 \ln 2} = 3.15 \text{ arcsec}^2 \quad (3)$$

for the high-resolution image ($\theta_{\text{maj}} = 2''.26$ and $\theta_{\text{min}} = 1''.23$). Note that Σ_{mol} depends only on the mass-to-light conversion factor $X_{\text{CO}} \propto \Sigma_{\text{mol}}/I_{\text{CO}} \propto M_{\text{mol}}/L_{\text{CO}}$, where L_{CO} is the CO (1-0) luminosity. The total molecular gas mass corrected for He and heavy elements is $\Sigma_{\text{mol}} = 1.41 \Sigma_{\text{H}_2}$ for the fractional abundance of hydrogen nuclei of 71%.

The measured flux density at the galactic center ($34.5 \text{ Jy beam}^{-1} \text{ km s}^{-1}$) yields a peak surface density of $\Sigma_{\text{mol}}^{\text{max}} = 1.1 \times 10^3 M_\odot \text{ pc}^{-2}$ if the low conversion factor $X_{\text{CO}} = 0.8 \times 10^{20} \text{ cm}^{-2} (\text{K km s}^{-1})^{-1}$ is applied (Salak et al. 2014). In the central 1-kpc region, we derived azimuthally averaged surface density Σ_{mol} as a function of radius by using the MIRIAD task ELLINT to find average flux densities in rings and then applied equation 2. The result is shown in figure 11; the high surface density of $\Sigma_{\text{mol}} = (10^2 - 10^3) M_\odot \text{ pc}^{-2}$ is typical for starburst galaxies (Kennicutt 1998) and implies a column density of $N_{\text{H}} = (10^{22} - 10^{23}) \text{ cm}^{-2}$ that explains the obscured nature of the central region. The parameters used to determine the ellipses were $PA = 324^\circ$, $i = 58^\circ$ (derived in section 4.1), and radius increments of $\Delta R = 1.13''$ (equal to $\theta_{\text{maj}}/2$). The resulting curve can be fit with two Gaussian functions of the form $a \exp[-(R - b)^2/(2c)^2]$ that correspond to the nuclear concentration (CND) and the ring. The offset parameter becomes $b_{\text{CND}} = 0''$ for the CND (corresponding to the galactic center) and $b_{\text{ring}} = 9''$ for the ring. This radius corresponds to 469 pc, which we adopt as the radius of the ring. The standard deviations are $c_{\text{CND}} = 2''$ (104 pc) and $c_{\text{ring}} = 3''.9$ (203 pc).

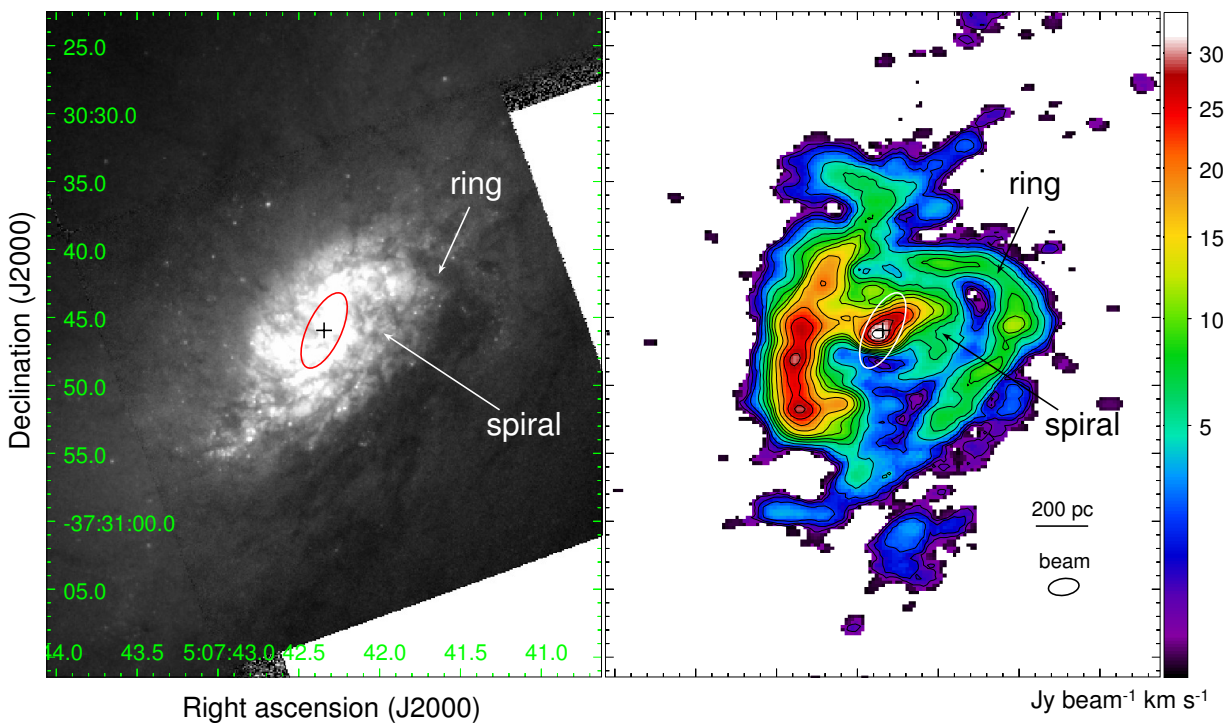


Fig. 10.— *Left.* HST *R*-band image (Hubble Legacy Archive). The black cross marks the position of the 2.8-mm continuum peak. The 500-pc ring and nuclear spiral are indicated with arrows; the ellipse in the center marks the region of the nuclear bar. *Right.* Distribution of the CO (1-0) integrated intensity displayed on a square root scale from $0.127 \text{ Jy beam}^{-1} \text{ km s}^{-1}$ (pixels below 5σ in this high-resolution image, where $1 \sigma = 10 \text{ mJy beam}^{-1}$, were masked) to the peak value of $34 \text{ Jy beam}^{-1} \text{ km s}^{-1}$ with contours at 0.5, 1, 2, 4, 6, 8, 10, 12, 16, 20, 24, 28, $32 \text{ Jy beam}^{-1} \text{ km s}^{-1}$. The synthesized beam ($2''.26 \times 1''.23$) is shown at the bottom right corner.

Table 5: Lower limits^a of CO (1-0) fluxes and molecular gas masses.

Region	Flux [Jy km s ⁻¹]	Mass [M_{\odot}]	X_{CO} [cm ⁻² (K km s ⁻¹) ⁻¹]	Fraction
$r_{\text{CND}} < 250$ pc (4''8)	281	1.4×10^8	0.8×10^{20}	
		3.4×10^8	2.0×10^{20}	0.18
$r_{\text{ring}} < 780$ pc (15'')	1224	6.0×10^8	0.8×10^{20}	
		1.5×10^9	2.0×10^{20}	0.80
Total image	1521	1.9×10^9	2.0×10^{20}	1.00

^aThe data are not corrected for missing short baselines. The fluxes are calculated by using the high-sensitivity data cube clipped at 4σ where $1\sigma = 5.5$ mJy beam⁻¹.

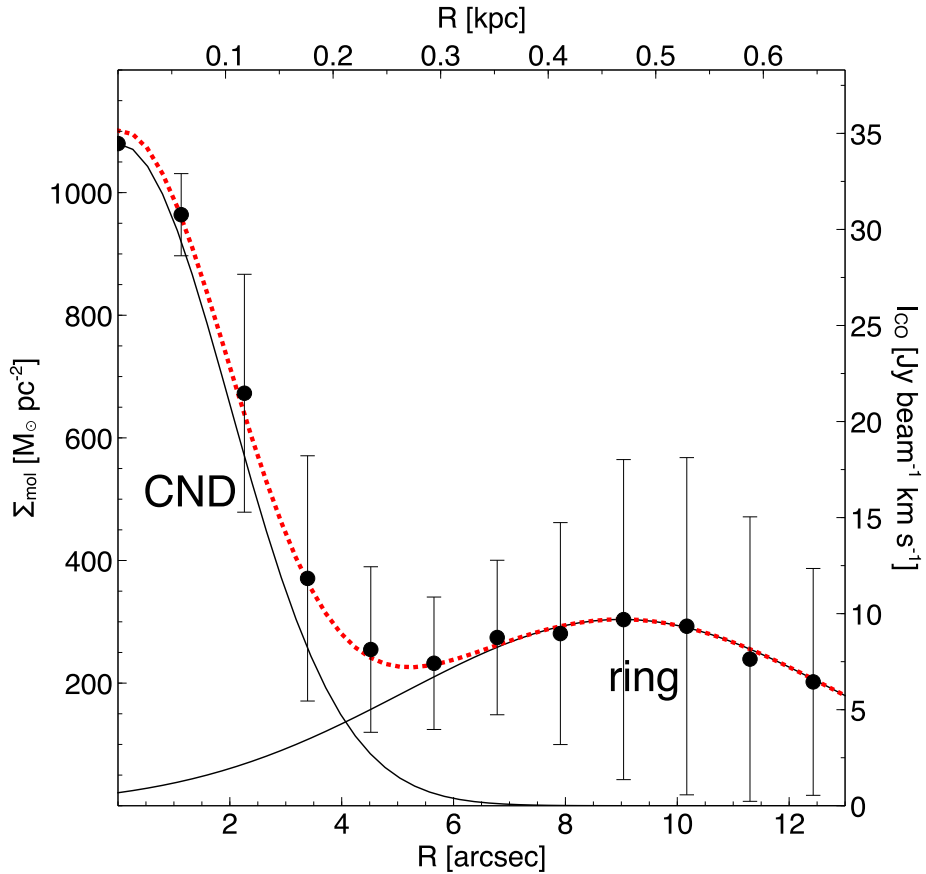


Fig. 11.— Molecular gas surface density (or integrated flux density) averaged over azimuth as a function of radius, $\Sigma_{\text{mol}}(R)$. The data are fit with two Gaussian functions representing the circumnuclear disk (CND) and the 500-pc ring.

3.3. Kinematics

3.3.1. Global properties

The high-sensitivity image presented in section 3.2 allows us to extract information on GMC velocities in the galactic disk and large-scale bar. An intensity-weighted velocity field image (moment 1), defined as $M_1 = \sum \mathcal{S}_i v_i / M_0$, is shown in figure 12. Intensity images integrated over narrow velocity bins (channel maps) of the entire mosaic and the central 2' region are shown in figures 13 and 14, respectively. In addition to large-scale rotation, molecular gas in the bar region exhibits peculiar motion evident as a large velocity gradient over the entire ridges on the leading side of the bar. This was noticed in HI data by Koribalski et al. (1996), and we show that CO is following a similar trend. The velocity field in the offset ridges shows a velocity gradient (shear) of $v_{\text{sh}} \equiv \Delta v / \Delta l \sim 0.2 \text{ km s}^{-1} \text{ pc}^{-1}$, or $\Delta v \sim 100 \text{ km s}^{-1}$ across the $\Delta l \sim 500 \text{ pc}$ wide ridges (in azimuthal direction perpendicular to the galactocentric radius).

3.3.2. Velocity field and dispersion in the central 1 kpc

The velocity field (moment 1) in the central region is shown in figure 15 (left). It appears slightly distorted, with the largest deviation $\sim 3''$ south and south-west of the center. Note the overall “S”-shape pattern, typical in galaxies with bars.

The velocity dispersion of molecular gas, defined as the second moment of intensity, $M_2 = \sqrt{\sum \mathcal{S}_i (v_i - M_1)^2 / M_0}$ (where M_0 and M_1 are the zeroth and first moments defined above), is shown in figure 15 (right). On average, M_2 is high (above 40 km s^{-1}) in the nucleus and decreases to $10\text{-}20 \text{ km s}^{-1}$ in the central disk. It rises again to $15\text{-}25 \text{ km s}^{-1}$ in the 500-pc ring and then decreases once more beyond the ring in the galactic disk.

Velocity dispersion can be an indicator of cloud (orbit) crowding. The dispersion is especially high ($\sigma > 40 \text{ km s}^{-1}$) north and north-east of the nucleus. By inspecting the CO spectra in this region (figure 16), we find double peaks within the synthesized beam ($\Delta l \simeq 90 \text{ pc}$). These features are not obvious in moment 1 images because the velocity is intensity-weighted. The moment 1 images do, however, show the S-shape and a steep velocity gradient north and south of the 500-pc ring. The profiles of the emission lines are somewhat affected by missing short-spacing baselines, but such effects cannot produce the observed line width because the negatives and sidelobes are weak. Note that this region is where the gas in the outer x1 orbits of the bar passes close to the 500-ring, where we expect to find an inner Lindblad resonance (ILR) and x2 orbits (section 4.2.2). The large

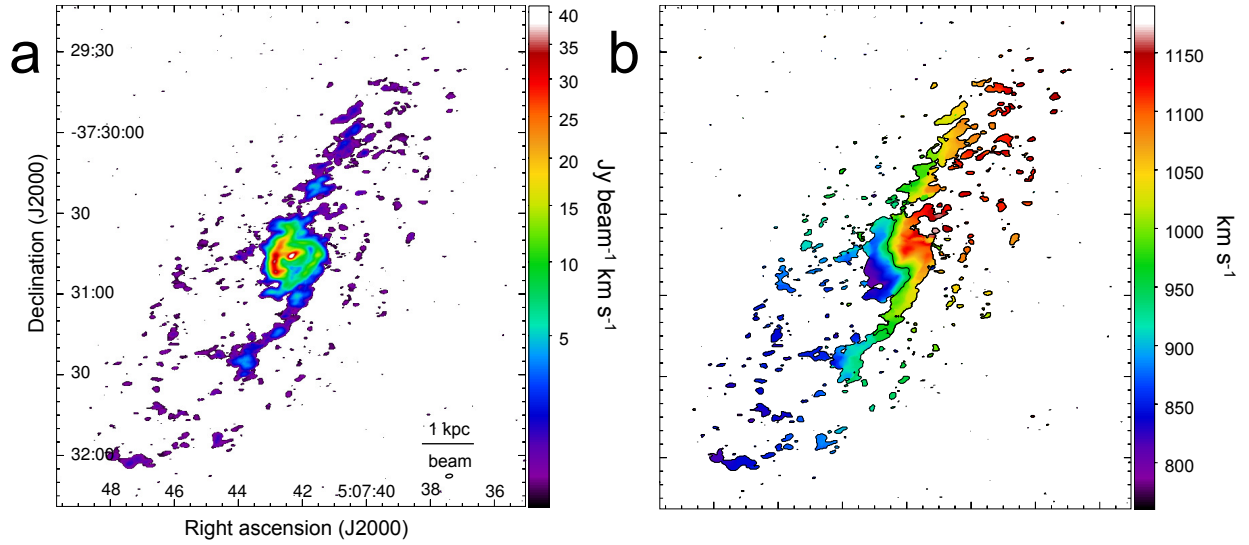


Fig. 12.— CO (1-0) integrated intensity (a), as in figure 7, and intensity-weighted velocity field (b) (moment 1) displayed from $v_{\text{LSR}} = 760$ to 1190 km s^{-1} on a linear scale. The central contour is plotted at $v_{\text{LSR}} = 964 \text{ km s}^{-1}$.

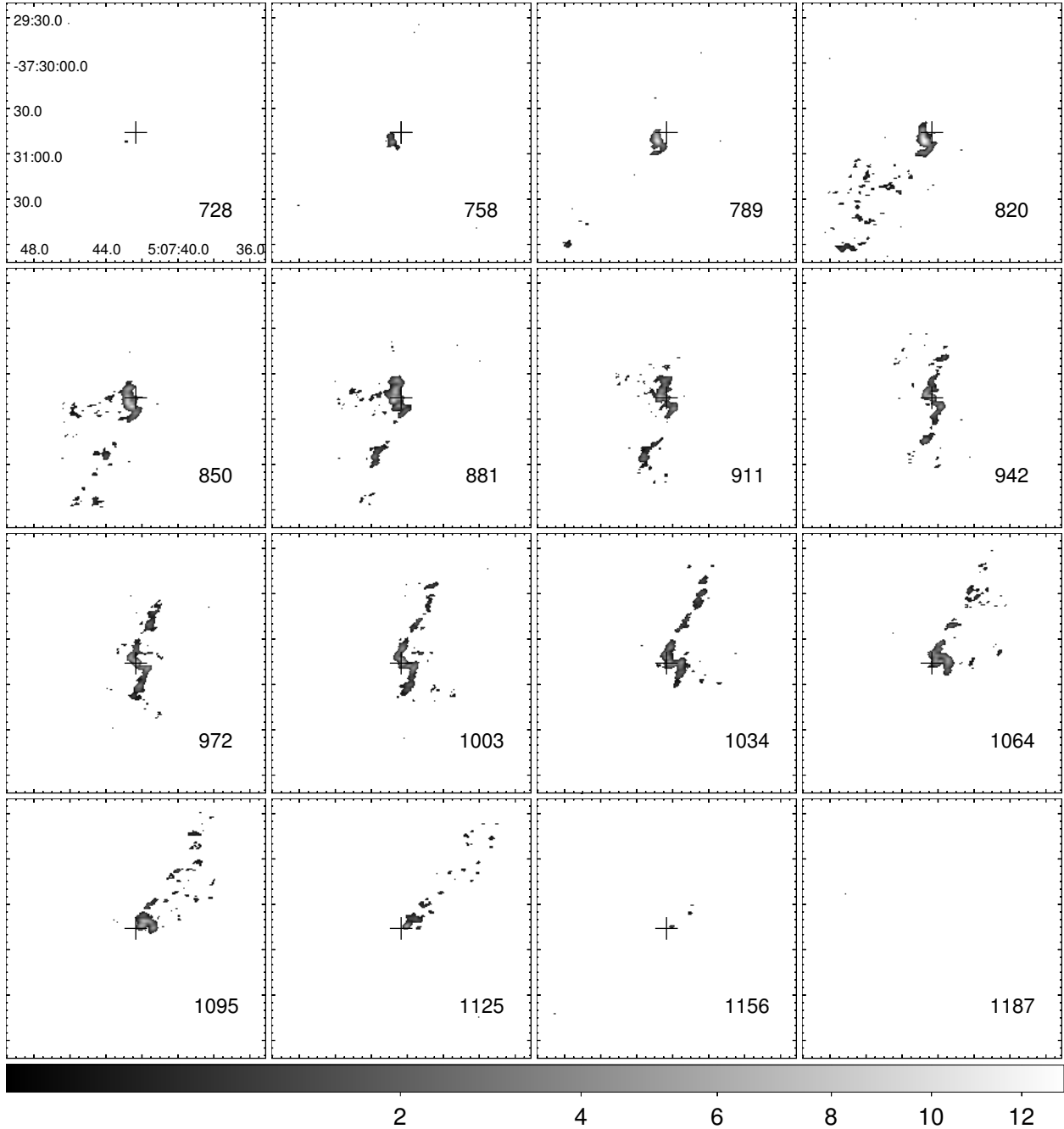


Fig. 13.— Channel maps of the entire image - integrated intensity maps of three subsequent channels (separations of 30.6 km s^{-1}) starting from 728 km s^{-1} ; the start channel velocity is shown at the bottom right corner of each image. The intensity is displayed on a square root scale identical for all images (from 0.22 to $13 \text{ Jy beam}^{-1} \text{ km s}^{-1}$; grey scale). The cross in each image marks the galactic center.

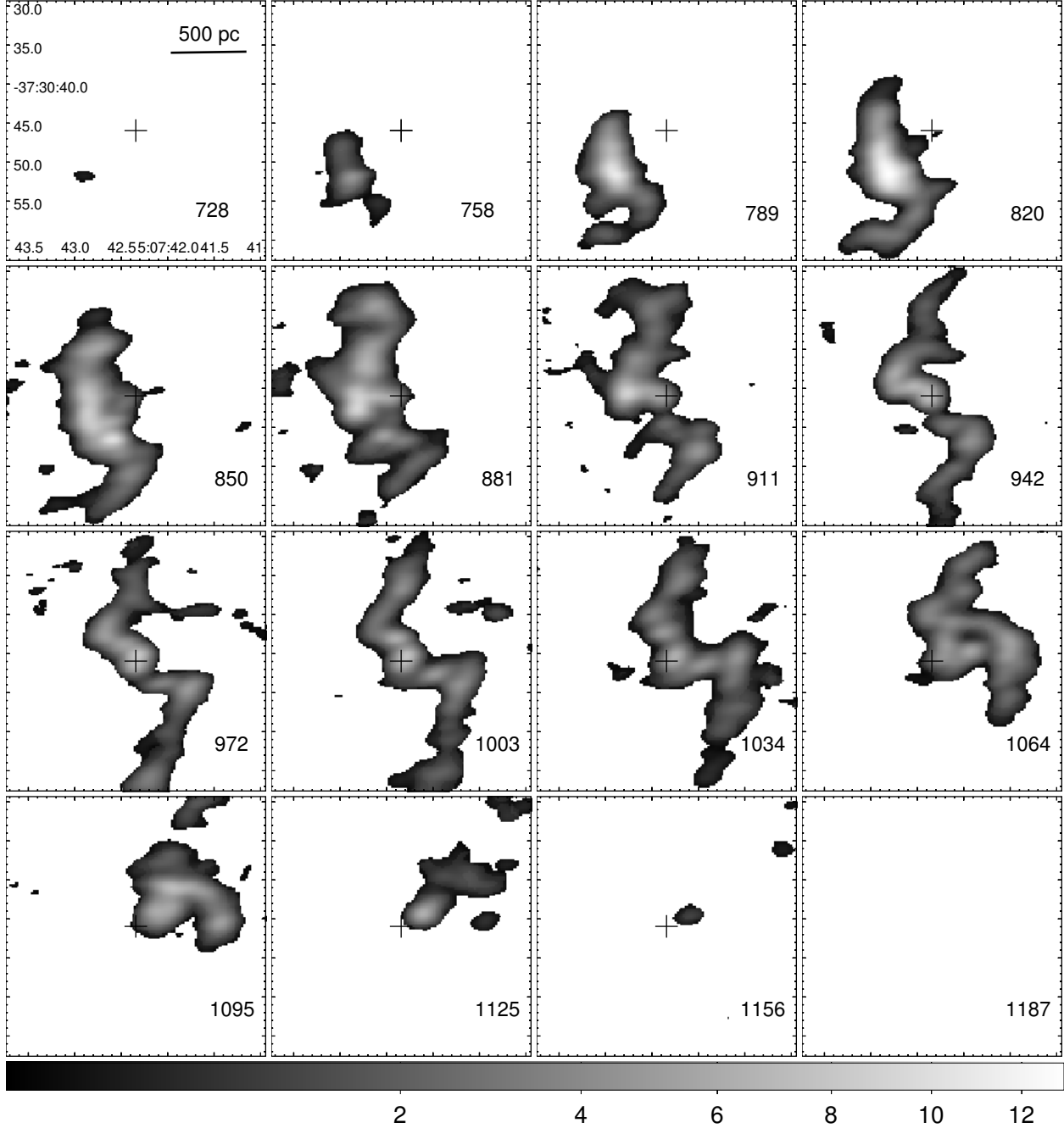


Fig. 14.— Same as figure 13 but showing the central region.

velocity widths (separations between the peaks in the spectra, $W \sim 100 \text{ km s}^{-1}$) indicate that the velocity gradient (shear) is high near the ILR, $v_{\text{sh}} \sim W/\Delta l \sim 1 \text{ km s}^{-1} \text{ pc}^{-1}$, a factor of several higher than in most of the ridge at larger radii. The gradient could disrupt the GMC structure, since the internal escape velocity of a cloud with radius $R = 10 \text{ pc}$ and $\Sigma = 200 M_{\odot} \text{ pc}^{-2}$ is $v_{\text{esc}} = \sqrt{2\pi GR\Sigma} \approx 7 \text{ km s}^{-1}$. The disrupted material may be in the form of low-density molecular gas unable to produce stars (e.g., Downes et al. 1996). We will see in section 6 that most of star-forming activity in NGC 1808 appears to be inside the ILR, consistent with this suggestion. A similar trend is observed at the south end of the ring too, although the emission is weaker and $W \approx 80 \text{ km s}^{-1}$.

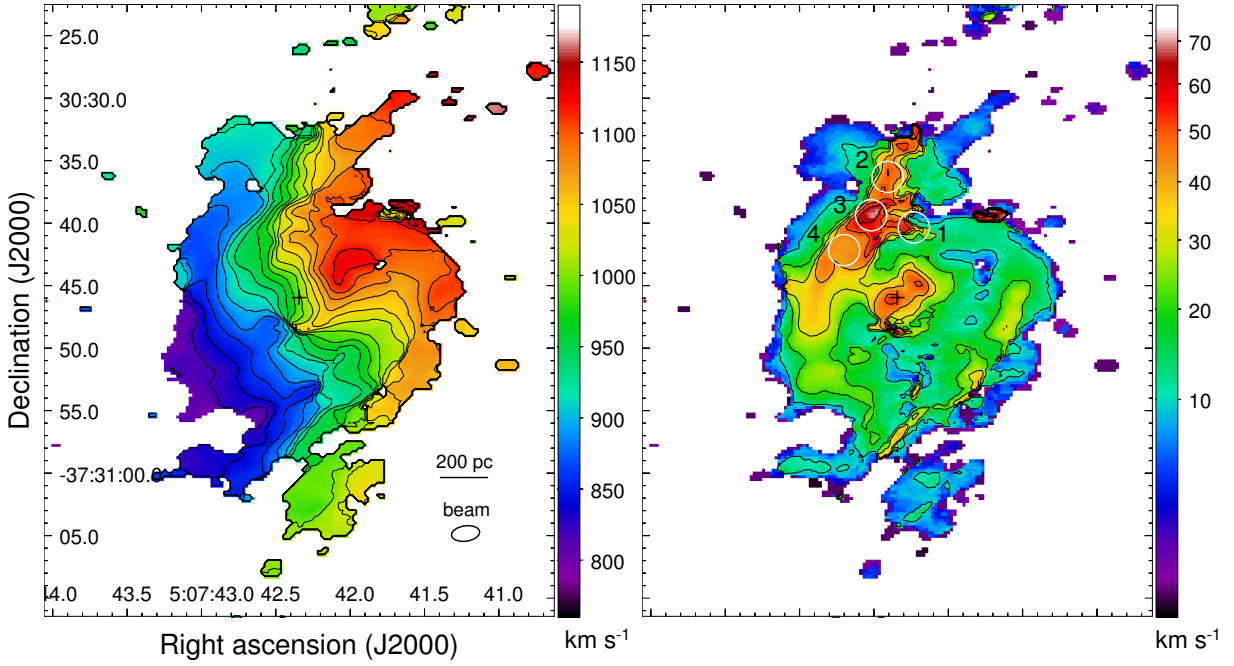


Fig. 15.— *Left*. Intensity-weighted velocity field of the central 1-kpc region with contours from $v_{\text{LSR}} = 820$ to 1140 km s^{-1} in steps of 20 km s^{-1} . *Right*. Velocity dispersion image displayed on a square root scale with contours from $\sigma_{\text{mol}} = 10$ to 60 km s^{-1} . Pixels below 5σ in this high-resolution image, where $1 \sigma = 10 \text{ mJy beam}^{-1}$, were masked. The black cross marks the position of the 2.8-mm continuum peak. The circles 1-4 (radius $1''.25$) indicate the regions where $\sigma_{\text{mol}} \sim 100 \text{ km s}^{-1}$ within the synthesized beam. The mean spectra within the circles are shown in figure 16.

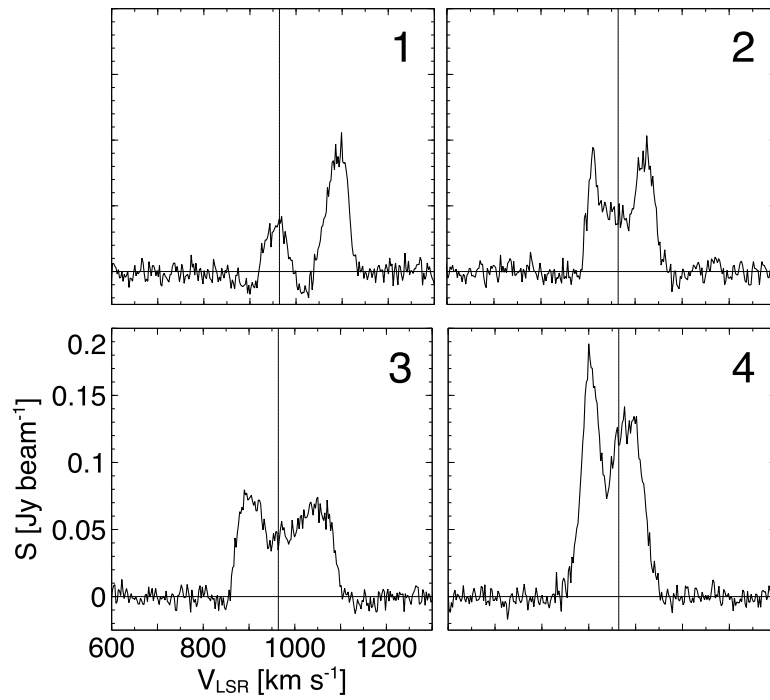


Fig. 16.— CO (1-0) spectra from the positions 1-4 in figure 15. The separations between the peaks within the synthesized beam ($\sim 90 \text{ pc}$) reach $\sim 100 \text{ km s}^{-1}$. The vertical line is plotted at $v_{\text{LSR}} = 964 \text{ km s}^{-1}$.

4. Gas dynamics

Detection of CO (1-0) in the central starburst region, kpc-scale bar, and spiral arms allows us to study gas dynamics in detail. In this paper, we focus primarily on the central 1-kpc region and derive basic geometric and kinematic parameters of molecular gas. On the large scale, we derive the bar pattern speed, and use it to locate the Lindblad resonances and corotation. Since the data presented here were taken with the 12-m array, i.e., without short-spacing baselines, extended structures such as arm/inter-arm regions and outflows are not fully sampled. We will discuss those features in detail in a future work that includes a short-spacing correction.

4.1. Derivation of geometric and kinematic parameters in the central 1 kpc

To determine the basic geometric and kinematic parameters of the central 1-kpc molecular zone, we used the program ^{3D}Barolo (3D-Based Analysis of Rotating Objects from Line Observations) that fits tilted-ring models to (3-dimensional) spectroscopic data (Di Teodoro & Fraternali 2015). The main parameters of the galaxy include the dynamical center at (x_0, y_0) , systemic velocity (v_{sys}), rotational velocity (i.e., rotation curve v_{rot}), gas velocity dispersion (σ_{mol}), galactic inclination (i), and position angle (PA). The program compares models with a data cube by fitting rings at various radii from the center. All parameters may vary from one ring to another, including inclination and position angle, thereby allowing a warp, i.e., a set of tilted rings with differential rotation (e.g., Rogstad et al. 1974). The computation, however, does not handle non-circular motion (e.g., radial motion due to spiral arm and bar dynamics, outflows from starburst and AGN feedback). The aim to use the program in this work is to fit circular motion components so that we can produce a model and then subtract it from the data. The residuals would reveal non-circular features.

4.1.1. Parameter computation

The high-resolution data cube ($\Delta v = 2.5 \text{ km s}^{-1}$) was used in this procedure. The calculation was carried out within 12 rings of equal width $\Delta r = 1''.13 = \theta_{\text{maj}}/2$ (where θ_{maj} is the FWHM of the synthesized beam along its major axis) from the center to $12''.4$ (646 pc), i.e., to the radius that comfortably covers the central molecular ring; beyond this radius the signal-to-noise ratio is low and the influence of the galactic bar is too high to derive reliable results by assuming circular orbits. The gas scale height (disk thickness) was kept as a non-free parameter at $h_z = 150 \text{ pc}$. In a disk with a Gaussian density profile perpendicular

to the galactic plane, this parameter is related to the gas velocity dispersion and surface density as $h_z = \sigma_{\text{mol},z}^2 (2\pi G \Sigma_{\text{mol}})^{-1}$, where $\sigma_{\text{mol},z}$ is the velocity dispersion in the z direction. For $\sigma_{\text{mol},z} = 20 \text{ km s}^{-1}$ and $\Sigma_{\text{mol}} = 300 M_{\odot} \text{ pc}^{-2}$, typical in the central region (e.g., figures 11 and 15), the scale height is $h_z \approx 150 \text{ pc}$. The parameter may vary by a factor of a few in the central region, though it makes negligible effect on the fitting result.

Although the program is able to guess all the parameters as functions of radius r simultaneously, we constrained the computations by providing the central position (x_0, y_0) to be the location of the peak of 2.8-mm continuum emission (assuming that it coincides with the low-luminosity AGN candidate). This is a reasonable choice because the CO peak has been found offset from this position and more extended than the continuum source. Unlike continuum, CO is likely to exhibit a torus structure that can be offset [e.g., in the Seyfert galaxy NGC 1068; Krips et al. (2011) and García-Burillo et al. (2014)]. In addition, we have constrained the galactic inclination to the literature value of $i = 57^{\circ} \pm 5^{\circ}$ (table 1), where the uncertainty is included to allow the program freedom to explore a range of 10° .

4.1.2. *Systemic velocity*

The program estimated the systemic velocity as a non-free parameter. This is calculated as the mid-point between the velocities that correspond to the 20% of the peaks of the CO (1-0) line profile. The profile within the central $40'' \times 40''$ box ($2.08 \times 2.08 \text{ kpc}^2$) is shown in figure 17 together with a spectrum of CO (3-2) acquired with the single dish telescope ASTE (Salak et al. 2014). The derived systemic velocity is $v_{\text{sys}} = 963.9 \pm 2.5 \text{ km s}^{-1}$ within the central region, in agreement with previously reported values measured with a large telescope beam that did not resolve the central 1-kpc region (965 km s^{-1} ; Aalto et al. 1994). A similar value of $965 \pm 5 \text{ km s}^{-1}$ was derived when we applied the fitting procedure on the ASTE CO (3-2) data cube and when the center position was not fixed.

Note that the CO line profiles exhibit a triple peak in the central region (figure 17). The triple peak can be decomposed into the 500-pc ring and nucleus. It is clear from the CO (1-0) spectrum of the central $r < 2''.5$ in figure 17 that the central peak corresponds to the nucleus. Applying the same procedure of systemic velocity computation, we fit 3 rings at radius increments that correspond to the beam width up to 235 pc (two times the major axis of the beam FWHM) and find a best fit at $v_{\text{sys}} = 998.4 \pm 2.5 \text{ km s}^{-1}$, more than 30 km s^{-1} higher than v_{sys} derived from global kinematics. This discrepancy, first noticed by Burbidge & Burbidge (1968), is also obvious in the position-velocity diagrams discussed below (figure 24).

A comparison of the CO (1-0) and CO (3-2) spectra in figure 17 can be used to estimate the missing flux in the ALMA data. Although the ratio of the intensities of the two lines, defined as $R_{31} \equiv I_{3-2}/I_{1-0}$, varies on small scale, Aalto et al. (1994) and Salak et al. (2014) found that, on average, $R_{31} \approx 0.6$ in the central kiloparsec. Then, one should multiply the CO (3-2) spectrum in figure 17 to obtain a CO (1-0) spectrum corrected for the short-spacing baselines. The resulting missing flux in the ALMA data could be as high as $\sim 40\%$ in the central 2 kpc region. Although the unrecovered flux is substantial, we note that this is likely much lower at the scale of the CND ($2''$), which is ten times smaller than the maximum recoverable scale of the imaging ($21''$). Also, the presence of the central peak in the single dish spectrum at a velocity shifted from the global systemic velocity by $\sim 30 \text{ km s}^{-1}$ suggests a kinematic offset.

Another method to calculate v_{sys} is to use a dense gas tracer in the central galactic region. The HCN (4-3) line profile acquired with ASTE (see Appendix) was fitted with a Gaussian function that yielded a peak velocity of $998.6 \pm 3.3 \text{ km s}^{-1}$, consistent with the nuclear component of the ALMA CO (1-0) spectrum and the central peak in the CO (3-2) spectrum. This velocity is also consistent with estimates from optical studies [e.g., nuclear heliocentric velocity of 1020 km s^{-1} in Véron-Cetty & Véron (1985) and Phillips (1993)] Therefore, for the central galactic region ($r < 235 \text{ pc}$), we suggest that the higher v_{sys} is appropriate.

The origin of the kinematic offset is not clear. One possibility is that the bulge is composed of two components: a massive inner component that dominates the dynamics of gas in the CND, and a larger component that determines the gas motion in the central 2 kpc, and that these two do not have a single dynamical center, possibly a consequence of a tidal interaction in the past (also evident as a warped outer ring; e.g., Koribalski et al. 1993).

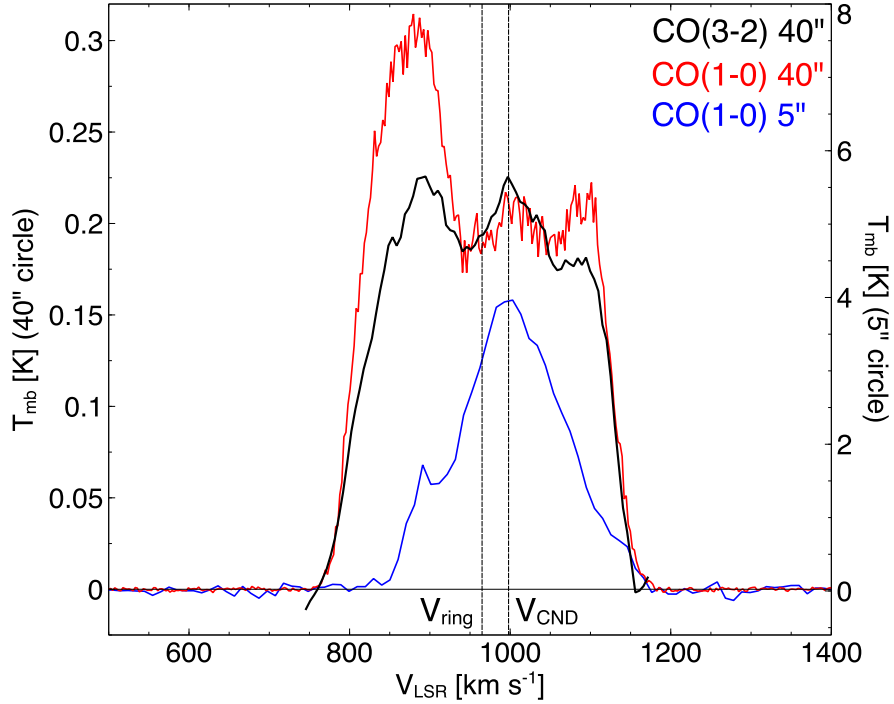


Fig. 17.— Mean CO (3-2) spectrum acquired with ASTE (black), and CO (1-0) spectrum from the ALMA data presented in this work (red) plotted as the mean brightness temperature within the central $r < 20''$. The ALMA data were smoothed to the resolution of $22''$ to match that of ASTE. Also shown is the ALMA CO (1-0) spectrum within $r < 2''.5$ (blue) at the original resolution (vertical axis on the right). Note the triple peak in the large-aperture spectra.

4.1.3. Position angle

The position angle is determined by finding a line that maximizes the velocity gradient in the observed image. The computation constrained PA to the range of $302^\circ < PA < 320^\circ$ (when $v_{\text{sys}} = 998 \text{ km s}^{-1}$), as shown in figure 18. In the central $r < 400 \text{ pc}$, the best fit is found for $\langle PA \rangle \simeq 316^\circ$. By applying the same method to derive PA for $v_{\text{sys}} = 964 \text{ km s}^{-1}$, an average value of 324° was found – the central region exhibits a warp of $\sim (5^\circ\text{--}10^\circ)$ from the CNB to the 500-pc ring. The position angle (and inclination) are consistent with the results based on HI data within $r \lesssim 120''$. The position angle remains $PA \sim 300^\circ$ until $r \sim 300''$, whereas inclination gradually decreases beyond $r \gtrsim 120''$ reaching $i \sim 30^\circ$ at $r \sim 300''$; this is manifested as the warped outer ring (Koribalski et al. 1993). To compare this result with the distribution of stars in the galactic bulge, we fitted the 2MASS K_s -band image (figure 7b) with a two-dimensional Gaussian function within the central $r < 30''$. The resulting PA was $323:69 \pm 0:48$, remarkably close to that derived from CO for $v_{\text{sys}} = 964 \text{ km s}^{-1}$. We adopt the value of 324° for the major axis of the 500-pc ring and galactic bulge.

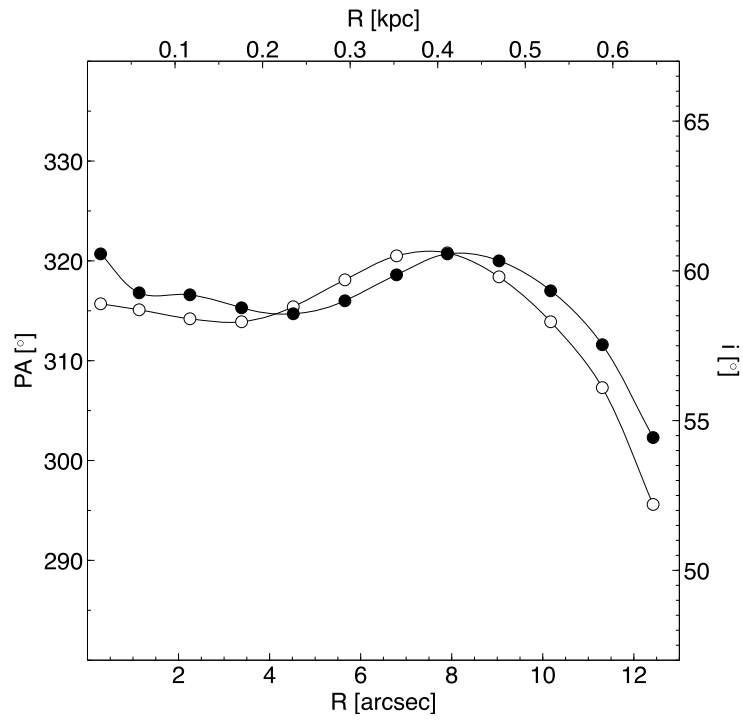


Fig. 18.— Position angle (filled circles) and inclination (open circles) derived by using the systemic velocity $v_{\text{sys}} = 998 \text{ km s}^{-1}$.

4.1.4. Rotation curve and dynamical mass

High-resolution CO line observations are useful for deriving rotation curves and mass distributions in the central regions of galaxies (e.g., Sofue & Rubin 2001; Sofue 2013). CO gas is often abundant and detectable with ALMA in the central regions where HI emission is weak and H α affected by extinction. The data presented in this work have high resolution and sensitivity to probe the gas kinematics in the galactic bulge region with spatially continuous CO detection from the nucleus to the 500-pc ring. We first derive a rotation curve (v_{rot}) by using ^{3D}Barolo and then analyze its composition.

The rotation curve derived by computation using $v_{\text{sys}} = 998 \text{ km s}^{-1}$ is plotted in figure 19. It can be decomposed into three parts: the nucleus ($r < 1''$), a steep rise at $1'' < r < 3''$, and a more gentle rise beyond that radius. This change of slope is not a consequence of change in i or PA because these parameters are calculated separately and included in the derivation of v_{rot} . The last three measurement points are less reliable because the 500-pc ring exhibits a different systemic velocity of 964 km s^{-1} and because gas dynamics is dominated by streaming motion in the global bar. The outermost values, however, are in agreement with HI data from Koribalski et al. (1993) and the result in Sofue et al. (1999) within uncertainty. The rotational velocity at the radius of $r = 705 \text{ pc}$, derived by using the systemic velocity $v_{\text{sys}} = 964 \text{ km s}^{-1}$, is $v_{\text{rot}} \simeq 215 \text{ km s}^{-1}$. The results of modeling of gas kinematics inside the nuclear ring (derived by using $v_{\text{sys}} = 998 \text{ km s}^{-1}$) are summarized in table 6.

Assuming a simple spherically symmetric mass distribution, the derived rotational velocity yields a dynamical mass of $M_{\text{dyn}}(r < 705 \text{ pc}) = rv_{\text{rot}}^2/G \simeq 7.5 \times 10^9 M_{\odot}$. By comparison, the total velocity-integrated flux in the same region is $S_{\text{CO}} = 991 \text{ Jy km s}^{-1}$ and the molecular gas mass derived by using the CO-to-H₂ conversion factor $X_{\text{CO}} = 0.8 \times 10^{20} \text{ cm}^{-2}(\text{K km s}^{-1})^{-1}$ becomes $M_{\text{H}_2} \simeq 5 \times 10^8 M_{\odot}$ [see also Salak et al. (2014) for a derivation using CO (3-2)]. The dynamical mass distribution is shown as a function of radius in figure 19 (right).

Next, we try to decompose the mass distribution into components that can explain the observed rotation curve. Since the rotation curve sampled at fine spacing of $1''.13$ shows extreme changes in slope that require multiple mass components and are likely affected by non-circular motion (effective on a scale of $\lesssim 2''$; section 4.2 and figure 24), we “smooth” the curve by re-deriving the velocity at increments of $2''.26$ (equal to θ_{maj}). The resulting curve can be fit by a crude model of two massive systems in the central 1 kpc. The larger one is the stellar bulge, while the smaller one denoted by major core (scale radius 95 pc) can be a simplified version of the nuclear bar and the molecular CND, which has a mass of $\gtrsim 1.4 \times 10^8 M_{\odot}$ in the central 300 pc and should be included in velocity curve calculations. The bulge and major core are represented by a simple Plummer sphere model (Plummer

1911) with the total gravitational potential given by

$$\Phi(r) = -\frac{GM_1}{\sqrt{r^2 + a_1^2}} - \frac{GM_2}{\sqrt{r^2 + a_2^2}}. \quad (4)$$

Here, \mathcal{M}_1 and \mathcal{M}_2 are the total masses, and a_1 and a_2 the scale lengths of the bulge and major core, respectively. The mass distribution of a Plummer sphere with the total mass \mathcal{M} is

$$M(< r) = 4\pi \int_0^r r'^2 \rho(r') dr' = \frac{\mathcal{M}r^3}{(r^2 + a^2)^{3/2}}, \quad (5)$$

where $\rho(r) = 3\mathcal{M}(1 + r^2/a^2)^{-5/2}(4\pi a^3)^{-1}$ is the volume density. Due to spherical symmetry, the rotational velocity is simply

$$v(r) = \sqrt{\frac{GM(< r)}{r}} = \sqrt{\frac{GM}{(r^2 + a^2)^{3/2}}}r. \quad (6)$$

The total rotation curve due to both systems, expressed as $v_{\text{rot}}(r) = \sqrt{v_1^2(r) + v_2^2(r)}$, is plotted in figure 20. We also include a nuclear star cluster with mass $\mathcal{M}_C = 1.4 \times 10^7 M_\odot$ and scale radius $a_C = 4.5$ pc, indicated from high infrared luminosity of the core (e.g., Oliva et al. 1995; Tacconi-Garman et al. 1996; Galliano & Alloin 2008). The selected scale radius corresponds to a core radius (where the surface density drops to the half of its maximum) of $r_c = \sqrt{\sqrt{2} - 1}a \approx 3$ pc, a typical value for nuclear clusters in nearby galaxies (Walcher et al. 2005). The derived mass of the bulge+major core ($\mathcal{M}_B = 1.32 \times 10^{10} M_\odot$) is consistent within 5% with the bulge mass derived by Sofue et al. (1999) by decomposing a kpc-scale rotation curve. In addition, a rotation curve that includes a tentative central supermassive black hole (mass $\mathcal{M}_{\text{BH}} = 1.2 \times 10^7 M_\odot$, or about thrice as massive as the Galactic one; Gillessen et al. 2009) is shown too; the black hole has a Keplerian rotation curve. It is not clear whether NGC 1808 has a supermassive black hole in its center, but figure 20 shows that it would not be distinguished from the star cluster of the same mass at the present resolution of 100 pc. For a bulge mass of $\mathcal{M}_{\text{B1}} = 1.25 \times 10^{10} M_\odot$, the black-hole-to-bulge mass ratio is of the order $\mathcal{M}_{\text{BH}}/\mathcal{M}_{\text{B1}} \sim 1 \times 10^{-3}$, consistent with large samples in Kormendy & Ho (2013). Note that even if a black hole and a nuclear cluster coexist as a core² of mass

²Supermassive black holes and nuclear clusters seem to coexist in many galaxies and the ratio of their masses can vary by three orders of magnitude. In the Galaxy, the mass of the black hole is only $\sim 15\%$ of the mass of the nuclear cluster, while in our neighbour M31, the black hole is ~ 4 times more massive. For a review, see Kormendy & Ho (2013) and the references therein.

$\mathcal{M}_{\text{core}} = \mathcal{M}_{\text{BH}} + \mathcal{M}_{\text{C}}$, the core-to-bulge mass ratio $\mathcal{M}_{\text{core}}/\mathcal{M}_{\text{B1}}$ also scales in agreement with Kormendy & Ho (2013) for composite nuclei. Higher-resolution data will resolve the nucleus and clarify whether the central rise of the rotation curve identified in figure 19 is due to a black hole or a nuclear star cluster. In either case, the rise of the rotation curve within $r < 1''$ reveals an embedded molecular gas disk or torus with a radius less than 50 pc. An exponential disk and dark halo components are not included here because their contributions are small at $r < 500$ pc. The disk would raise the rotation curve at larger radii, but due to the presence of a galactic bar, detailed modeling of the bar potential would be required to probe rotation beyond the 500-pc ring. The parameters of the model are shown in table 7.

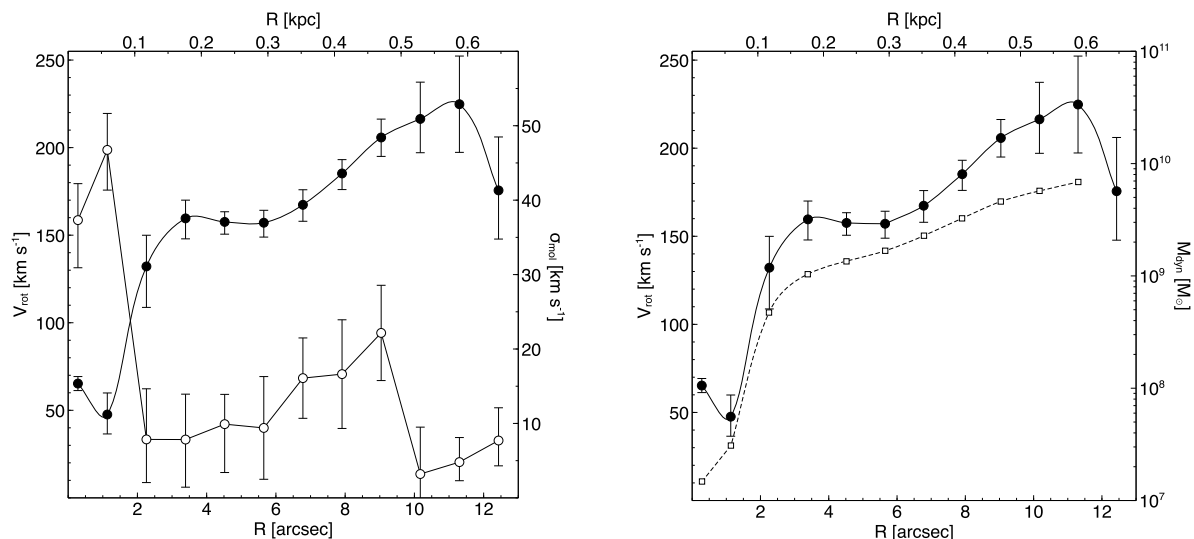


Fig. 19.— *Left.* Rotation curve (v_{rot} , full line) sampled in rings of width $\Delta R = 1''.13$ within $R < 676$ pc. It was determined by using the nuclear systemic velocity $v_{\text{sys}} = 998 \text{ km s}^{-1}$ (filled circles) and corrected for the inclination and position angle (figure 18). Also plotted is the gas velocity dispersion (σ_{mol} , open circles). *Right.* Rotation curve and dynamical mass distribution (M_{dyn} , dashed line).

Table 6: Geometric and kinematic parameters of the central 1-kpc molecular zone.

Ring	Radius ["]	Radius [pc]	v_{rot} [km s^{-1}]	σ_{mol} [km s^{-1}]	i [$^{\circ}$]	PA [$^{\circ}$]
1	0.28	15	$65.3^{+4.0}_{-4.0}$	$37.3^{+4.9}_{-6.4}$	58.9	320.7
2	1.13	59	$47.6^{+12.3}_{-11.1}$	$46.7^{+4.9}_{-5.4}$	58.7	316.8
3	2.26	117	$132.2^{+17.8}_{-23.4}$	$7.9^{+6.8}_{-5.8}$	58.4	316.6
4	3.39	176	$159.6^{+10.4}_{-11.7}$	$7.8^{+6.1}_{-6.4}$	58.3	315.3
5	4.52	235	$157.6^{+5.8}_{-7.0}$	$9.9^{+4.0}_{-6.5}$	58.8	314.7
6	5.65	294	$157.1^{+7.1}_{-8.2}$	$9.4^{+6.9}_{-6.9}$	59.7	316.0
7	6.78	353	$167.3^{+8.6}_{-9.4}$	$16.1^{+5.4}_{-5.4}$	60.5	318.6
8	7.91	411	$185.2^{+7.9}_{-9.2}$	$16.6^{+7.3}_{-7.3}$	60.6	320.7
9	9.04	470	$205.8^{+10.5}_{-10.8}$	$22.2^{+6.4}_{-6.4}$	59.8	320.0
10	10.17	529	$216.4^{+21.0}_{-19.3}$	$3.2^{+6.3}_{-6.3}$	58.3	317.0
11	11.30	588	$224.8^{+27.5}_{-27.5}$	$4.8^{+3.3}_{-2.5}$	56.1	311.6
12	12.43	646	$175.6^{+30.5}_{-27.8}$	$7.7^{+4.4}_{-3.4}$	52.2	302.3

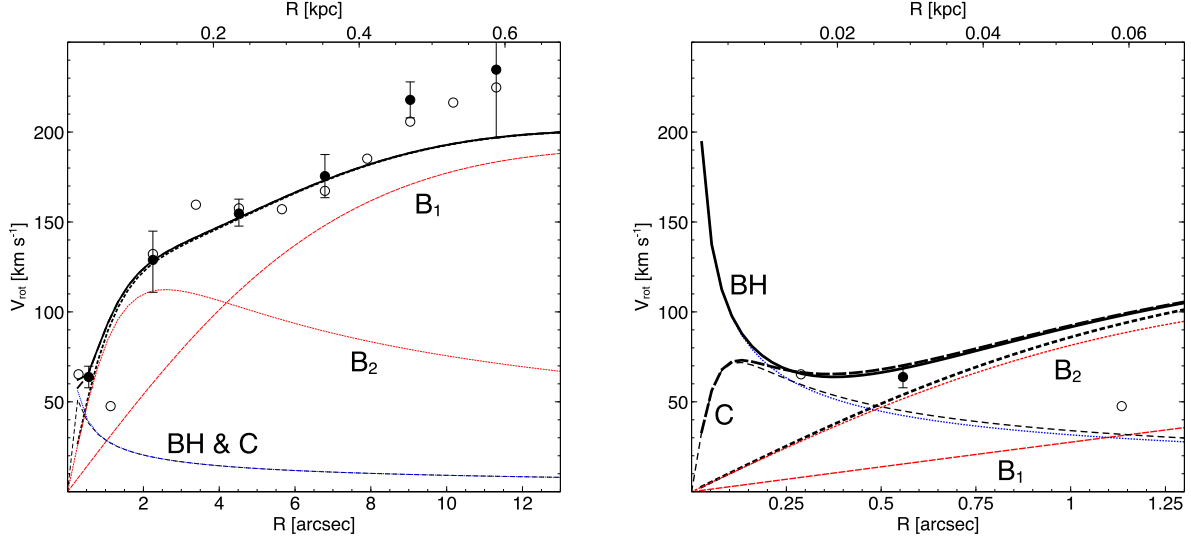


Fig. 20.— *Left.* Rotation curve within $R < 676$ pc fitted with three Plummer spheres and a black hole (Keplerian rotation). The curves represent: bulge (B_1) and major core (B_2) plotted with red dotted lines, nuclear cluster (C , dashed thin line), black hole (BH , blue dotted line), total curve with B_1 and B_2 only (dotted thick line), total curve including C (dashed thick line), and total curve including BH (full thick line). The open circles are the data from figure 19, while the filled circles are the data from the smoothed curve. *Right.* Enlargement of the central 68 pc of the diagram in the left panel.

Table 7: Dynamical parameters of the galactic model in the central 1 kpc.

Component	$\mathcal{M} [M_\odot]$	a [pc]	$\Sigma_s(0) [M_\odot \text{ pc}^{-2}]$
Bulge (B_1)	1.25×10^{10}	575	1.2×10^4
Major core (B_2)	7.2×10^8	95	2.0×10^4
Nuclear bar (NB)	5.8×10^8	95	2.0×10^4
Nuclear cluster (C)	1.4×10^7	4.5	2.20×10^5
Central black hole (BH)	(1.2×10^7)	–	–
Total	1.32×10^{10}		2.52×10^5

4.1.5. Stellar surface density in the nucleus

In order to compare our mass estimate based on gas dynamics with the total mass budget of the old stars in the central region, we used *I*-band (F814W filter on *Hubble Space Telescope*) and *K_s*-band [ISAAC on *Very Large Telescope*; Galliano & Alloin (2008)] images shown in figure 21. High-resolution *I*-band images have been useful in estimating black hole masses in nearby galaxies (Davis et al. 2013; Onishi et al. 2015), whereas the *K_s*-band image is a good choice because it is unaffected by dust extinction. The images were used to derive the radial profiles of surface brightness, $I(R) = L/D^2$ (L is the luminosity and D is the physical size of the observed region), and estimate the total stellar surface density in the central $r < 250$ pc, assuming a uniform mass-to-light ratio $M(r)/L(r)$. To do this, we normalized the peaks of the radial profiles to the peak of the surface density derived by using gas dynamics. For the Plummer sphere model discussed above, the stellar surface density is calculated as

$$\Sigma_s(R) = \int_{-\infty}^{\infty} \rho[r(z)] dz = 2 \int_{-\infty}^{\infty} \frac{3a^2 \mathcal{M} dz}{4\pi(a^2 + z^2 + R^2)^{5/2}} = \frac{a^2 \mathcal{M}}{\pi(a^2 + R^2)^2}, \quad (7)$$

where $z = \sqrt{r^2 - R^2}$ is the axis along the line of sight, and R is the projected radius in the plane of the sky. The results are given in table 7, and the total surface density due to the bulge and nuclear bar, $\Sigma_s = \Sigma_{B1} + \Sigma_{NB}$, is plotted in figure 22 along with the normalized flux profiles of the near-infrared images. The mass of the nuclear bar is calculated as $\mathcal{M}_{NB} = \mathcal{M}_{B2} - \mathcal{M}_{CND}$, where $\mathcal{M}_{CND} = 1.4 \times 10^8 M_\odot$ (table 5). To deal with the central peak, we added a nuclear star cluster (mass \mathcal{M}_C and surface density Σ_C calculated using equation 7) to match the normalized flux peak (assuming at this point that the near-infrared emission is dominated by starlight rather than hot dust). The total surface density profile is then $\Sigma_s = \Sigma_{B1} + \Sigma_{NB} + \Sigma_C$. The obtained Σ_s is a good match for the observed surface brightness, except in a region that appears like an arc or a spiral arm at $r \sim 200$ pc marked in figure 21, suggesting that the mass of the core can be dominated by a compact stellar system. Furthermore, if the nucleus has undergone a starburst episode with a star formation rate of $SFR \sim 1 M_\odot \text{ yr}^{-1}$ over the past $t_{SB} \sim 10^7$ yr, as estimated by Krabbe et al. (1994), it is reasonable to expect a star cluster at the galactic center with a mass comparable to \mathcal{M}_C .

Alternatively, the central peak in the infrared images could be due to emission from dusty ISM heated to high temperatures by a low-luminosity AGN. In that case, the peak would be the product of a convolution of the AGN-dominated region with the point spread function (PSF) of the telescope. In the simplest case, the AGN is a point source (delta function), the PSF is a Gaussian, and the resulting convolution is equal to the PSF. Using the PSF of

the K_s -band image, it is possible to reproduce the central peak in surface brightness shown in figure 22 (right). However, the convolution of the PSF with the surface brightness of the compact cluster Σ_C can also result in a function similar to the PSF.

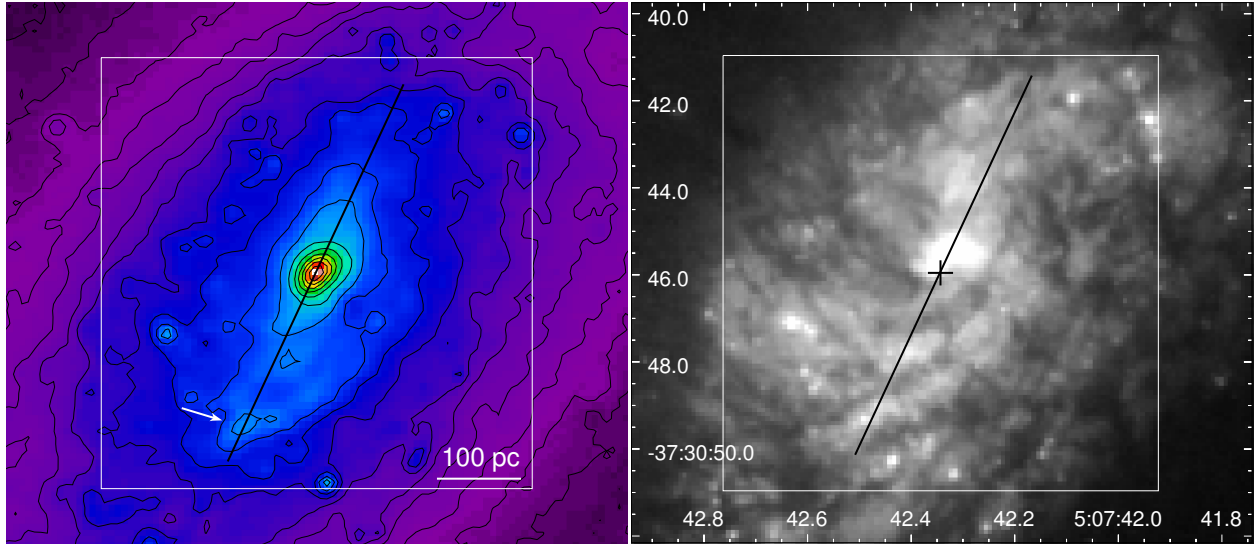


Fig. 21.— K_s -band (left) and I -band (right) images of the central region. The white rectangle shows the central $10'' \times 10''$. The black line is the projection slice at $PA = 335^\circ$ (orientation of the major axis of the nuclear bar) and length 500 pc. The white arrow marks the position of an arc-like feature (see figure 22).

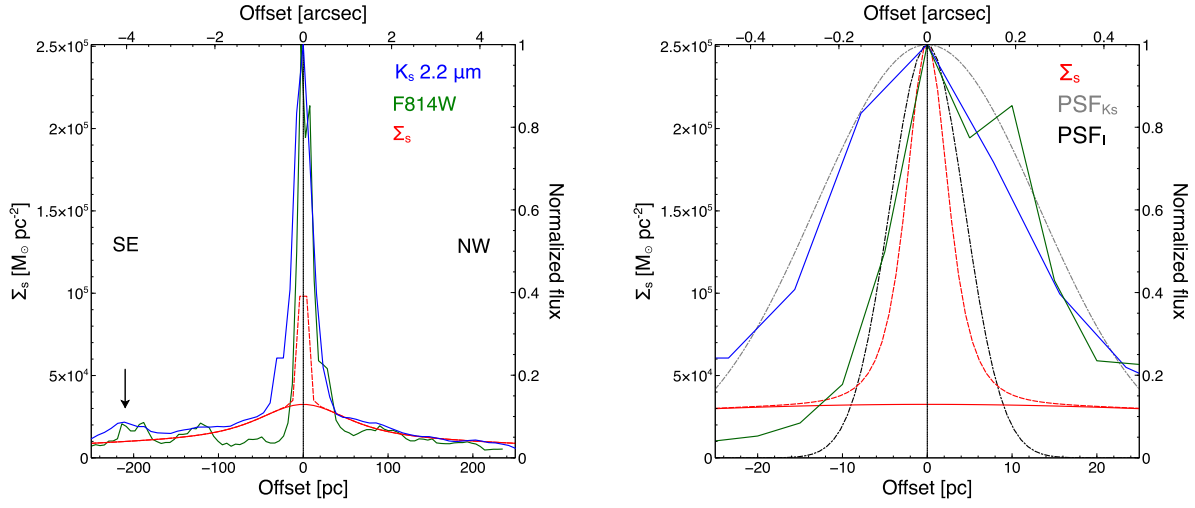


Fig. 22.— *Left.* Radial profiles of the normalized fluxes of the K_s (blue) and I (green) images plotted along a 500-pc slice (offset from the galactic center at $PA = 335^\circ$; figure 21). Also shown is the total surface density of old stars that comprises a bulge and nuclear bar (full red line: $\Sigma_s = \Sigma_{B1} + \Sigma_{NB}$) calculated from gas dynamics (table 7). The dashed red line (cut at 1/3 its maximum for clarity) shows the total surface density that includes a nuclear cluster ($\Sigma_s = \Sigma_{B1} + \Sigma_{NB} + \Sigma_C$). The arrow marks the location of an arc feature (also marked in figure 21). *Right.* Enlargement of the central 50 pc. The grey and black dot-dashed curves are the PSFs of the K_s -band and I -band images (FWHMs equal to $0''.6$ and $0''.2$, respectively).

4.2. Non-circular motions in the galactic disk

Gas kinematics can be further investigated with position-velocity diagrams (PVDs). PVDs along the major (X) and minor (Y) galactic axes can reveal azimuthal and radial streaming motions, respectively (e.g., Aalto et al. 1999). Using the parameters derived above, PVDs were plotted along the global kinematic major and minor axes at $PA_{\text{maj}} = 324^\circ$ and $PA_{\text{min}} = 54^\circ$, respectively (figure 23). The width of the slits is equivalent to the FWHM of the beam major axis.

The PVD along the major axis shown in figure 24a exhibits rotation that can be decomposed into three components (modeled in section 4.1.4): (1) rigid-body rotation within $r < 2''.5$, (2) nearly flat rotation curve within $2''.5 < r < 6''$, followed by (3) additional rise in velocity. Inspection of figure 25 shows that the deviation (1) is less prominent beyond $|Y| = 2''.5$ from the nucleus suggesting that it is confined to the central $r \lesssim 2''.5$, as expected from a massive core in the CND.

4.2.1. Velocity gradient along the minor axis

Figure 24b shows a PVD plotted along the minor axis ($X = 0''$) that reveals striking non-circular motions in the central 1-kpc region: the “zig-zag” pattern as a signature of a velocity gradient along the minor axis. As shown in the next section, the velocity offsets at $|Y| \gtrsim 8''$ correspond to a component dominated by the global bar dynamics. Non-circular motions appear least important in the region $4'' < |Y| < 7''$, where gas kinematics is dominated by circular rotation of the disk (highest-intensity emission in figure 24b). Irregular motions intensify again at $|Y| < 4''$, in the vicinity of nucleus.

The panels (c) and (d) of figure 24 show examples of fitting with ^{3D}Barolo: the red contour is the best fit obtained with a warp model superimposed on a the PVD diagram made from the data cube. We note that the program created a good fit for the major axis (panel c). The situation is, however, significantly different for the minor axis (panel d). The fit was successful only for the high-intensity emission that is near the systemic velocity (998 km s⁻¹), i.e., for the near-circular motion components. Since ^{3D}Barolo can handle warps in circular orbits by searching for symmetric features in the data cube, we regard the non-fitted emission in figure 24d as non-circular motion. Specifically, we recognise two patterns: (1) streaming motions in the SW with velocities $|v_{\text{LSR}} - v_{\text{sys}}| \sim 50 \text{ km s}^{-1}$ at $Y \approx -2''.5$ and $Y \approx -7''$ (marked with arrows in panel d), and (2) highly blueshifted component in the NE with $|v_{\text{LSR}} - v_{\text{sys}}| \sim 100 \text{ km s}^{-1}$ from $Y = 0''$ to $Y \approx 6''$. Most of the emitting gas on the NE side is near the systemic velocity (998 km s⁻¹) and there is signature of the zig-zag

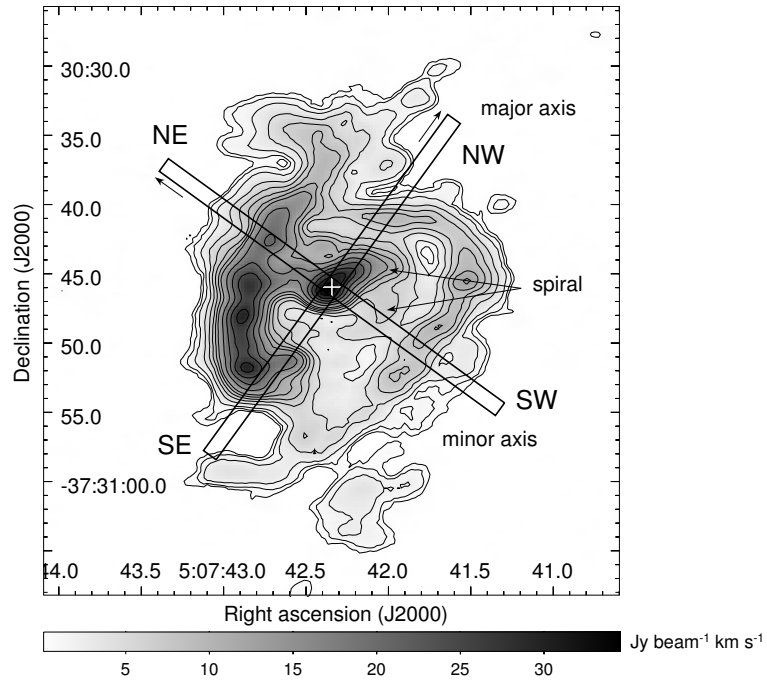


Fig. 23.— PVD slices plotted on the intensity image. Major ($PA = 324^\circ$) and minor ($PA = 54^\circ$) axes are indicated. The width of each slice is 9 pixels ($2''.25$), corresponding to the major axis of the beam FWHM. The length is $30''$ (1.6 kpc). Note the presence of a spiral arm between the CND and the 500-pc pseudo ring; the ring too extends as a two-arm pattern.

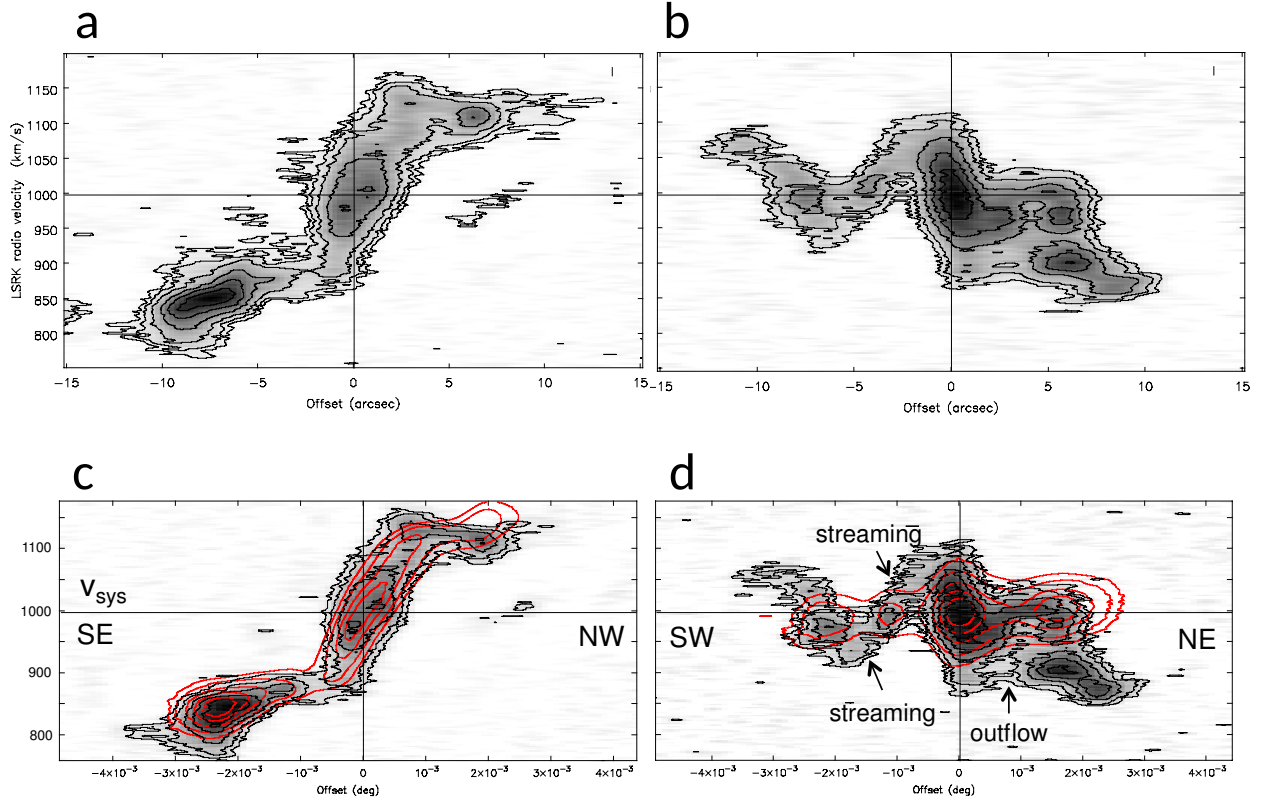


Fig. 24.— (a) PVD along the adopted major axis ($PA = 324^\circ$) at $Y = 0$ with the contours plotted at 0.05, 0.1, 0.2, 0.4, 0.6, 0.8 times the peak $0.36 \text{ Jy beam}^{-1}$. (b) PVD along the adopted minor axis ($PA = 54^\circ$) at $X = 0$ with the contours plotted at 0.1, 0.2, 0.4, 0.6, 0.8 times the peak $0.24 \text{ Jy beam}^{-1}$. Panels c and d show examples of fitting with $3^{\text{D}}\text{Barolo}$, where the red contours (normalized to 0.1, 0.2, 0.4, 0.6, 0.8 times the peak) are the best fits. The horizontal line is $v_{\text{LSR}} = 998 \text{ km s}^{-1}$. Streaming motion and outflow are indicated.

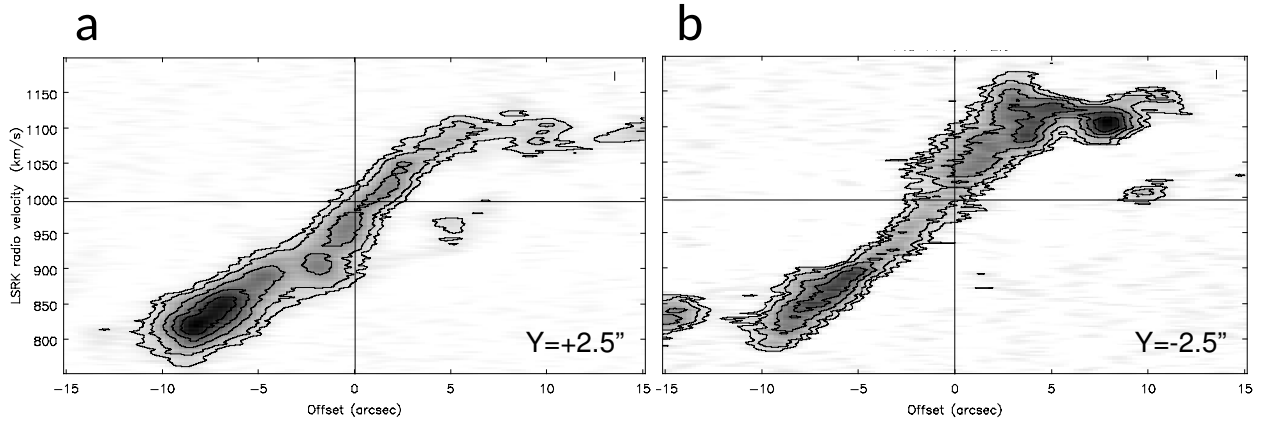


Fig. 25.— PVD parallel to the adopted major axis ($PA = 324^\circ$) at $Y = 2''.5$ (a) and $Y = -2''.5$ (b). The contours are plotted at 0.1, 0.2, 0.4, 0.6, 0.8 times the peak $0.24 \text{ Jy beam}^{-1}$. The horizontal line is $v_{\text{LSR}} = 998 \text{ km s}^{-1}$.

pattern, but the extreme velocities between $v_{\text{LSR}} = 870$ and 950 km s^{-1} [corresponding to $|v_{\text{LSR}} - v_{\text{sys}}| = (48 - 128) \text{ km s}^{-1}$] can be explained only as a large inflow in the disk or an outflow off the disk. We show below that the outflow scenario is more likely (section 5).

4.2.2. Bar pattern speed and Lindblad resonances

To investigate non-circular motions in the galactic disk, we created a model of a disk with pure circular rotation. The observed line-of-sight velocity v_{obs} in cylindrical coordinates (r, ϕ, z) is given by

$$v_{\text{obs}} = v_{\text{sys}} + v_{\phi} \sin i \cos \phi + v_r \sin i \sin \phi + v_z \cos i, \quad (8)$$

where v_{ϕ} is the rotational (azimuthal, ϕ component) velocity, v_r radial velocity, v_z vertical velocity (perpendicular to the galactic plane negative toward the observer), and ϕ the position angle measured with respect to the major galactic axis. The model velocity includes a rotation curve v_{rot} , and excludes radial and extraplanar motions ($v_r = v_z = 0$):

$$v_{\text{mod}} = v_{\text{sys}} + v_{\text{rot}} \sin i \cos \phi. \quad (9)$$

Subtracting the model velocity field from the data, we get a residual image,

$$v_{\text{res}} = (v_{\phi} - v_{\text{rot}}) \sin i \cos \phi + v_r \sin i \sin \phi + v_z \cos i, \quad (10)$$

that carries information about non-circular and extraplanar motions. Assuming that most of the emission originates in the galactic plane ($v_z = 0$), the residual image yields a relation between azimuthal and radial velocities. Note that negative values of v_{ϕ} correspond to blueshifted velocities in images.

The parameters used to generate a model velocity field for the central region are $PA = 316^\circ$ (mean value; section 4.1.3), $i = 58^\circ$, $v_{\text{sys}} = 998 \text{ km s}^{-1}$, and $v_{\text{rot}}(r)$ derived from numerical fitting described in subsection 4.1. In the case of a global model, we applied $PA = 324^\circ$, $i = 57^\circ$, $v_{\text{sys}} = 964 \text{ km s}^{-1}$, and a flat rotation curve of $v = 190 \text{ km s}^{-1}$ beyond $13''.6$, consistent with the global rotation curve (Sofue et al. 1999). The position angle and inclination are kept constant in the global model because in the central 1 kpc they vary with radius less than about 10° . The resulting residual velocity image is shown in figure 26. From the residual image, it is clear that the velocity of molecular gas in the offset ridges in the bar region deviates largely from the rest of the disk.

The position angle of the bar is $PA_b \approx 335^\circ$, hence only $\phi \approx 11^\circ$ with respect to the galactic disk. Because of this, radial motion ($v_r \sin i \sin \phi$) can be ignored along the bar in the residual velocity image given by equation 10. This is a favourable situation for deriving the bar pattern speed Ω_b using CO kinematics because equation 8 simplifies to $v_{\text{obs}} \approx v_{\text{sys}} + v_\phi \sin i$, where $v_\phi \approx r\Omega_b$ becomes the rotational velocity of the bar and is expected to linearly increase with r (e.g., Sakamoto et al. 2000; Kuno et al. 2000; Koda et al. 2002; Koda & Sofue 2006; Hirota et al. 2014). This trend is clear from the PVD in figure 27 where the offset ridges exhibit approximately linear behaviour. Measuring the velocities at emission peaks along the ridge within the bar ($1 \text{ kpc} \leq r \leq 3 \text{ kpc}$) and fitting with a least-squares method, we derive a bar pattern speed of $\Omega_b = 56 \pm 11 \text{ km s}^{-1} \text{ kpc}^{-1}$.

Using the rotation curve derived in section 4.1.4, it is possible to calculate the angular velocity Ω and investigate the dynamical resonances of stellar orbits in the galactic disk. The locations of Lindblad resonances are found from $m(\Omega - \Omega_b) = \pm\kappa$, where $\kappa = \sqrt{rd\Omega^2/dr + 4\Omega^2}$ is the epicyclic frequency of stellar orbits calculated as $\kappa \simeq \sqrt{2\Omega(\Omega + \Delta v/\Delta r)}$, and m is the rotational symmetry parameter (equal to 2 for a bar or two-arm pattern). Figure 28 shows Ω , $\Omega \pm \kappa/2$, $\Omega - \kappa/4$, and $\Omega_b = 56 \text{ km s}^{-1} \text{ kpc}^{-1}$, where the rotation curve v_{rot} was adopted from figure 20 at $r < 600 \text{ pc}$, and assumed constant, $v_{\text{rot}} = 190 \text{ km s}^{-1}$, at $r > 1.5 \text{ kpc}$ (Sofue et al. 1999). If the disk rotation is flat at $v_{\text{rot}} = (160\text{--}200) \text{ km s}^{-1}$, corotation occurs at $r_{\text{CR}} = v_{\text{rot}}/\Omega_b \simeq (2.9\text{--}3.6) \text{ kpc}$, and $r_{\text{CR}}/a_b \simeq (1.0\text{--}1.2)$, where a_b is the length of the semi-major axis of the bar (section 3.2.1). This result is consistent with theoretical predictions for weak bars (e.g., Contopoulos 1980; Athanassoula 1992a; Binney & Tremaine 2008). A weak bar is “allowed” to exist only between the inner Lindblad resonance (ILR), where $\Omega_b = \Omega - \kappa/2$, and the corotation radius r_{CR} , where $\Omega = \Omega_b$ (Binney & Tremaine 2008). From figure 28, the outer inner Lindblad resonance (oILR) appears at $(0.9\text{--}1.2) \text{ kpc}$. Additional ILRs are located near 450 pc where $\Omega - \kappa/2$ has a local minimum and intersects with Ω_b ; they coincide with the 500-pc ring. The rotation curve includes the contribution from a tentative massive black hole at the galaxy center. As a consequence, $\Omega - \kappa/2$ sharply rises within $r < 50 \text{ pc}$ [see, e.g., Combes et al. (2014) for NGC 1566]. There is also a resonance where $\Omega - \kappa/4$ intersects with Ω_b near $r \simeq 2.2 \text{ kpc}$; close to this radius in the SE ridge, we find a GMA and HII region (briefly discussed in section 3.2.1; figure 9).

4.2.3. Residual velocities in the central 1 kpc

In the nuclear region, the residual velocities of molecular gas, derived in the previous section and shown in figure 29, reveal the following patterns of non-circular motion (consistent with the PVD discussed in section 4.2.1). First, there is conspicuous streaming motion

with magnitudes $\sim 50 \text{ km s}^{-1}$ on the inner edge of the nuclear spiral arm ($2''$ – $3''$ south and south-west of the center). The magnitude of the streaming motion is comparable but larger than, e.g., in the grand-design spiral galaxy M51 by about a factor of two (Meidt et al. 2013). Second, north-east of the center, there is a blueshifted component spatially correlated with the extraplanar dust lane visible in the R -band (discussed in the next section). Finally, at radii of $r > 500 \text{ pc}$ in the NE and SW, the residual velocities abruptly reach $\sim 100 \text{ km s}^{-1}$; these features are related to the velocity gradient near the ILR, also apparent from the velocity field and dispersion images presented in section 3.3. A comparison with figure 26 shows that the large residuals extend along the ridges in the bar region.

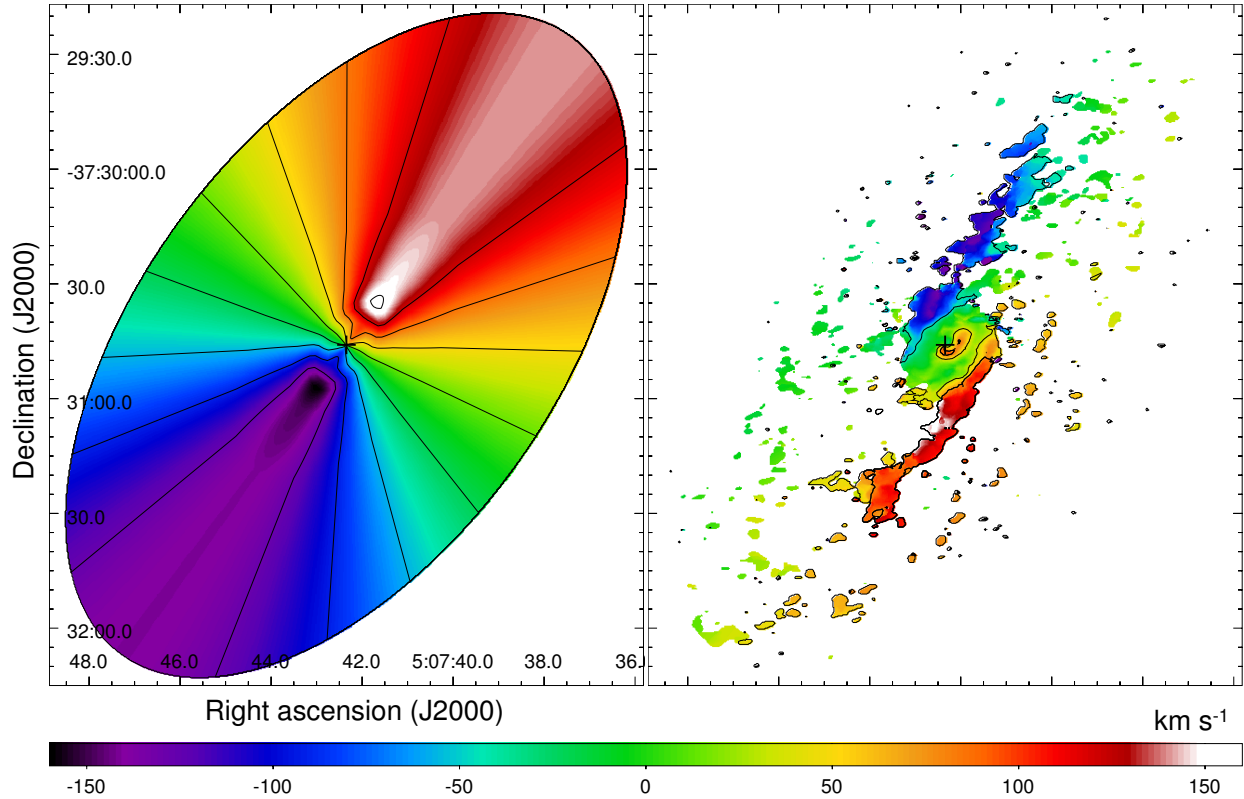


Fig. 26.— *Left.* Model velocity field (circular rotation) of the entire galaxy generated by using $v_{\text{sys}} = 964 \text{ km s}^{-1}$ and $PA = 324^\circ$. *Right.* Residual velocity image after subtracting the model from the observed data velocity. The contours are plotted at $-80, -40, 40, 80 \text{ km s}^{-1}$.

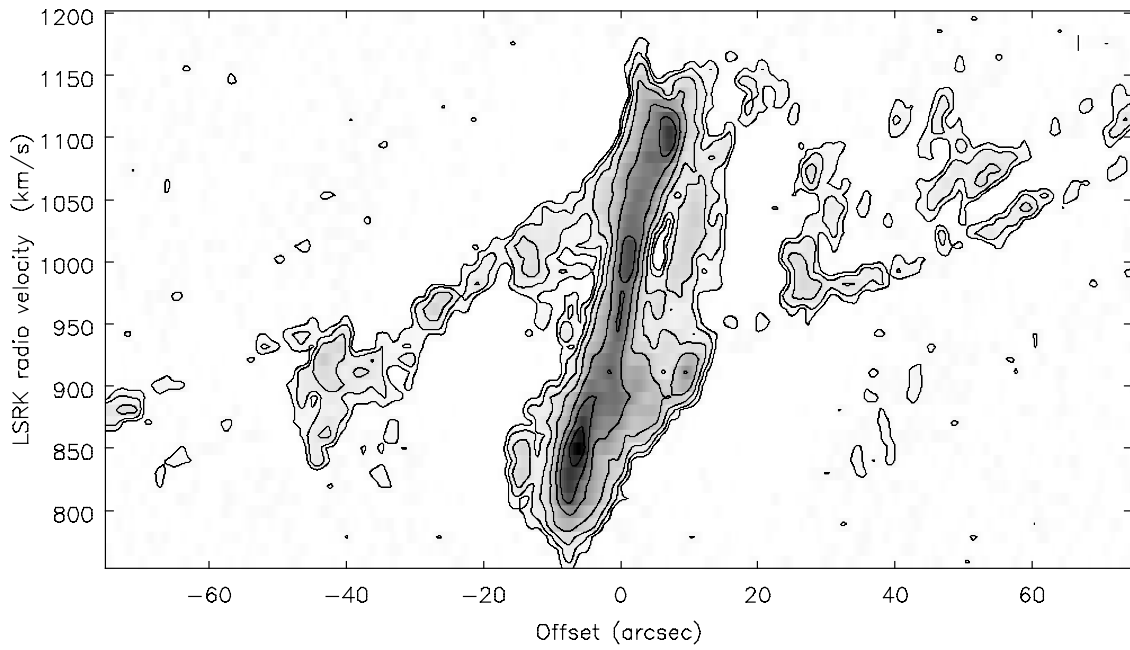


Fig. 27.— Position-velocity diagram along the bar major axis $PA_b = 335^\circ$ in the range $-75'' < X < 75''$. The thickness of the slit is 99 pixels ($25''$) and the contours are plotted at 0.025, 0.05, 0.1, 0.2, 0.4, 0.6, and 0.8 times $127 \text{ mJy beam}^{-1}$.

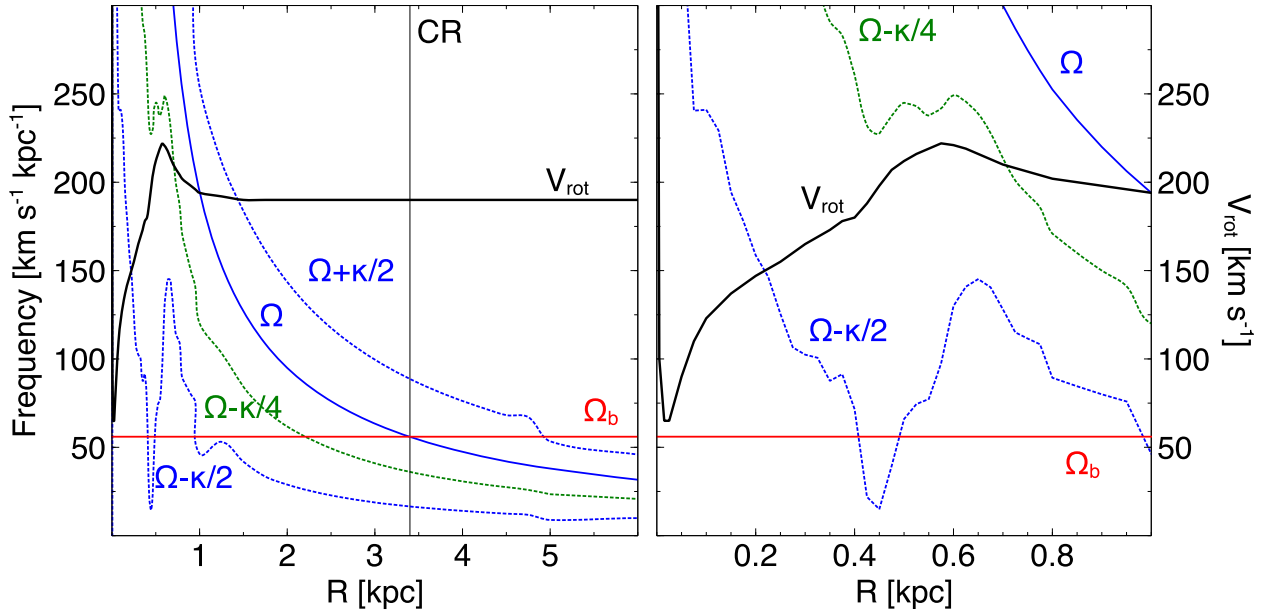


Fig. 28.— Orbital resonances in the inner 6 kpc (left) and 1 kpc (right). The rotation curve v_{rot} from figure 20 is assumed constant at $r > 190 \text{ km s}^{-1}$. The contribution from a tentative supermassive black hole is included. The vertical line CR marks the corotation radius.

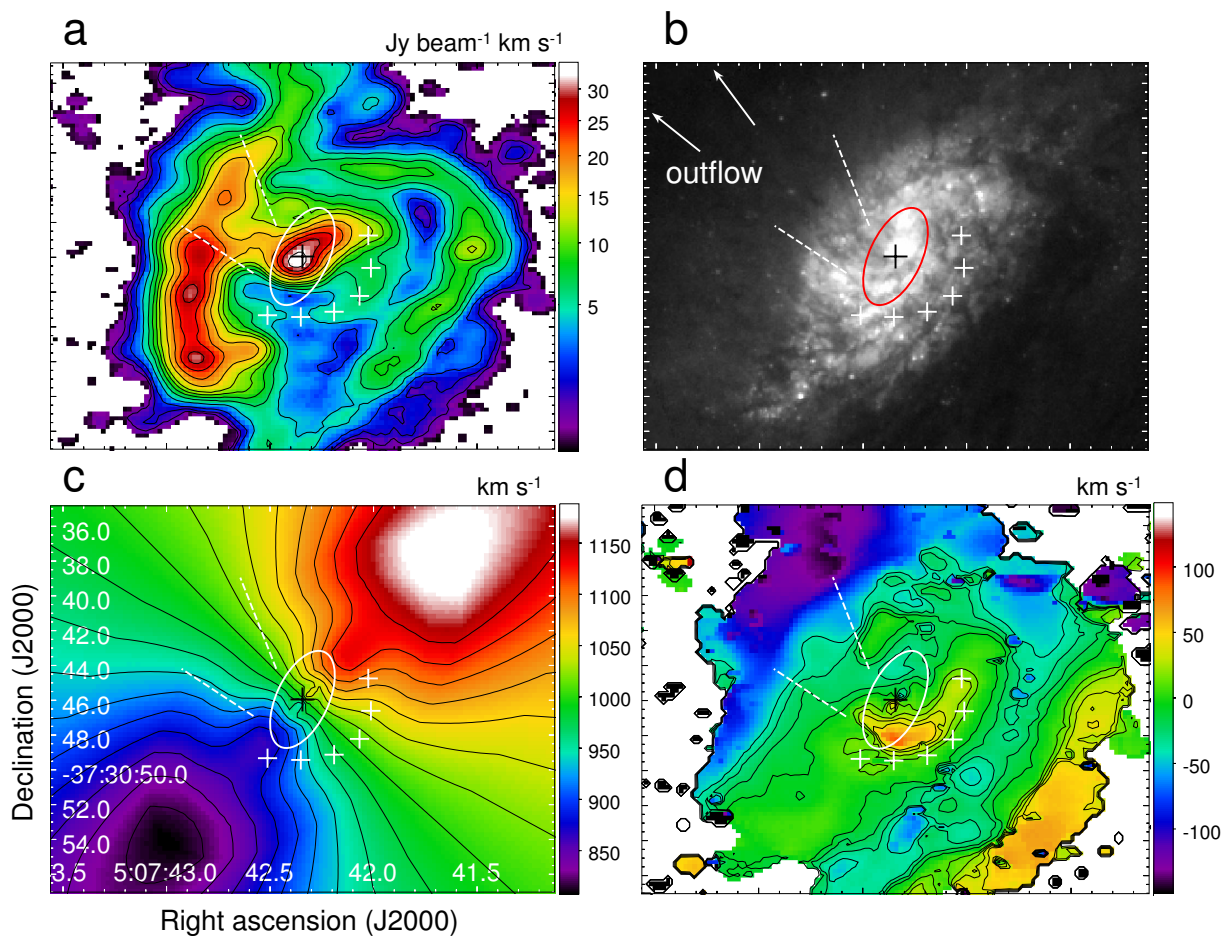


Fig. 29.— a) CO (1-0) integrated intensity (same as figure 10, right); b) HST image (cf. figure 1, right); c) model velocity field with circular rotation generated by using $v_{\text{sys}} = 998$ km s⁻¹, $PA = 316^\circ$, and the rotation curve derived in section 4.1.4; d) residual velocity field calculated by subtracting the model from the data. The contours are plotted at -40, -30, -20, -10, 10, 20, 30, 40 km s⁻¹. Note the non-circular motions as redshifted residual velocities up to ~ 80 km s⁻¹ on the inner side of the nuclear spiral arm (indicated by white crosses to guide the eye) and the blueshifted emission north-east of the center tracing the nuclear outflow (white dashed lines marking the orientation of the extraplanar dust lanes). Also conspicuous are the regions of streaming motion in the large-scale bar with residual velocities $\sim (50-100)$ km s⁻¹ in the NE and SW. The galactic center and nuclear bar are marked by a black cross and ellipse, respectively.

5. Molecular gas outflow

5.1. Morphology and kinematics

As shown in introduction, conspicuous dust lanes visible up to ~ 3 kpc above the galactic plane in optical images and the detection of NaI D in absorption and emission on opposite sides of the disk indicate the presence of a neutral gas outflow at velocities up to $v_{\text{out}} \sim 380$ km s $^{-1}$ (Phillips 1993). Furthermore, McCormick et al. (2013) found that the distribution of polycyclic aromatic hydrocarbons (PAHs) also extends into the halo to a similar distance, confirming the presence of a dusty wind. At the base of the outflow, recent integral-field observations revealed the presence of a cone of ionized gas (Sharp & Bland-Hawthorn 2010). Since the central region of the galaxy is predominantly in molecular phase, one might expect that CO-emitting gas is entrained in the superwind as observed in galaxies like M82 and NGC 253 (e.g., Salak et al. 2013; Bolatto et al. 2013a). Is there any evidence of a CO outflow in NGC 1808?

The optical image in figure 29b shows an extraplanar (polar) dust lane north-east of the nucleus, at a similar position angle as the kpc-scale dust lanes in figure 30a and the hot ionized cone revealed in the [NII]/H α ratio (Sharp & Bland-Hawthorn 2010). The location of the outflow with respect to other galactic structures is marked in figure 30b. We also show a comparison of an HST image with the CO (1-0) intensity distribution (high-sensitivity image) in figure 30 (panels c and d): there are four kpc-scale dust lanes denoted by L1-L4, all emerging from the central 1-kpc region. CO was not detected in the lanes L2-L4, except at their inner ends [base of the outflow; panel (c)]. The molecular gas is coincident, however, with an extraplanar dust lane L1 [panel (d)]. The L1 lane is blueshifted with respect to the systemic velocity ($v_{\text{LSR}} \approx 900$ km s $^{-1}$; see figure 31 and the blue wing in the spectrum of the central 5'' region in figure 17) as would be expected from an outflow, though there is no unambiguous redshifted counterpart on the opposite SW side [the asymmetry is also apparent in the optical line in Phillips (1993) and Sharp & Bland-Hawthorn (2010)]. Figures 30 and 31 show that L1 is coincident with a spur of CO (1-0) emission that extends beyond the 500-pc ring to around $(\alpha, \delta)_{\text{J2000}} = (5^{\text{h}}7^{\text{m}}43^{\text{s}}.2, -37^{\circ}30'42'')$. Enhanced velocity dispersion (figure 15) and the velocity width as wide as 150 km s $^{-1}$ along the minor axis north-east of the nucleus (figures 24 and 32 below) also indicate the presence of extraplanar gas. It is not clearly seen in the moment 1 image of figure 15 (left) because the velocity field is intensity-weighted and the extraplanar emission is spatially coincident with the underlying circular-rotation in the disk that dominates the overall CO (1-0) emission. Assuming a nuclear outflow perpendicular to the galactic plane, the average deprojected outflow velocity becomes (equation 8)

$$v_z = \frac{|v_{\text{obs}} - v_{\text{sys}}|}{\cos i} \simeq 180 \text{ km s}^{-1}, \quad (11)$$

where $i = 57^\circ$, $v_{\text{obs}} = 900 \text{ km s}^{-1}$, and $v_{\text{sys}} = 998 \text{ km s}^{-1}$ (section 4.1). Note that if this gas were in the galactic plane, the observed velocity would yield an inflow of $v_r = |v_{\text{obs}} - v_{\text{sys}}|/\sin i \simeq 117 \text{ km s}^{-1}$ inside the $r < 500 \text{ pc}$ disk, which is comparable to the rotational velocity. The derived outflow velocity is consistent with typical values found in superwinds in galaxies like M82 and NGC 253 [100-200 km s^{-1} ; e.g., Nakai et al. (1987); Walter et al. (2002); Salak et al. (2013); Bolatto et al. (2013a)]. Also, the detection of blueshifted emission NE from the center excludes the possibility of an extraplanar gas inflow. The opening angle of the outflow is uncertain, but the orientation of the dust lanes at the base of the outflow appears nearly perpendicular to the galactic major axis on optical images. The L4 lane reconnects with the galactic disk at a radius of $r \sim 3 \text{ kpc}$, indicating the gas motion as a fountain - the ejected ISM material falling back onto the galaxy [see Phillips (1993)]. The multitude of dust lanes is interesting because it suggests that extraplanar gas and dust may be confined to narrow regions as “filaments” in addition to the projected walls of a cylindric outflow as seen in, e.g., M82 (Nakai et al. 1987; Salak et al. 2013; Leroy et al. 2015).

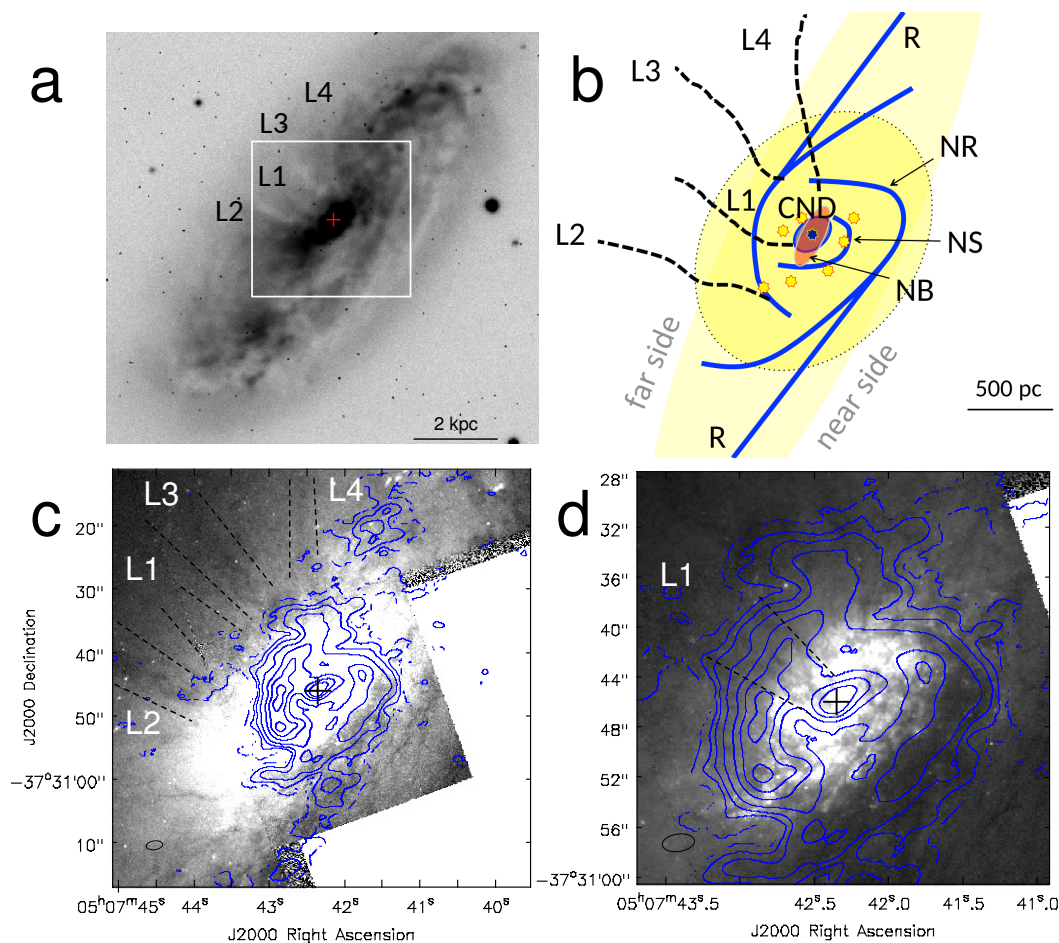


Fig. 30.— Morphology of the outflow with respect to the galactic structure in NGC 1808. (a) Large-scale R -band image (same as figure 1 with marked extraplanar dust lanes (L1-L4)). (b) Illustration of the structure in the central 2 kpc. The main components are: bulge (dotted yellow filled ellipse), primary bar (elongated large-scale yellow filled ellipse), molecular gas ridges in the bar (R), star-forming regions and supernova remnants (stars), 500-pc ring (NR), nuclear spiral arm (NS), nuclear bar (red ellipse; NB), circumnuclear disk (blue ellipse; CND), and outflow of gas and dust (black dashed lines; L1-L4). (c) HST R -band image of the central region [rectangle field in (a); same scale as (b)]. The blue contours are CO (1-0) plotted at 0.01, 0.05, 0.1, 0.2, 0.4, 0.6, 0.8 times the peak of $41 \text{ Jy beam}^{-1} \text{ km s}^{-1}$. The optical image was enhanced to emphasize the dust lanes outside the central region. (d) Enlargement of the field in (c) to show the nuclear outflow L1. The cross marks the galactic center.

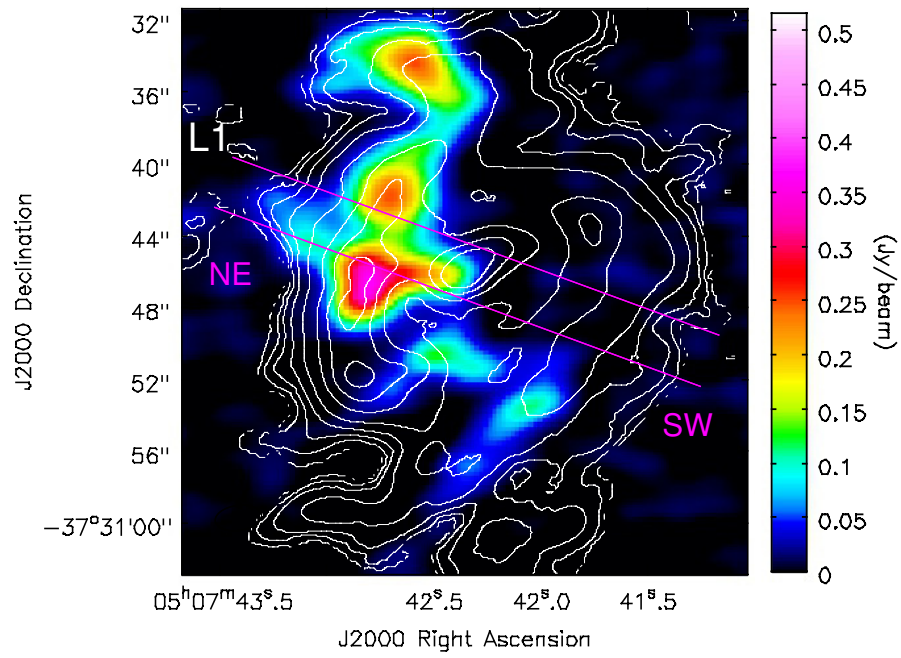


Fig. 31.— Channel map of the high-sensitivity CO (1-0) data cube at 911 km s^{-1} (color) with contours of the integrated intensity plotted at 0.01, 0.05, 0.1, 0.2, 0.4, 0.6, 0.8 times $41 \text{ Jy beam}^{-1} \text{ km s}^{-1}$. The magenta lines mark the PVD slice width ($3'25$) and orientation (70°). The resulting PVD is shown in figure 32.

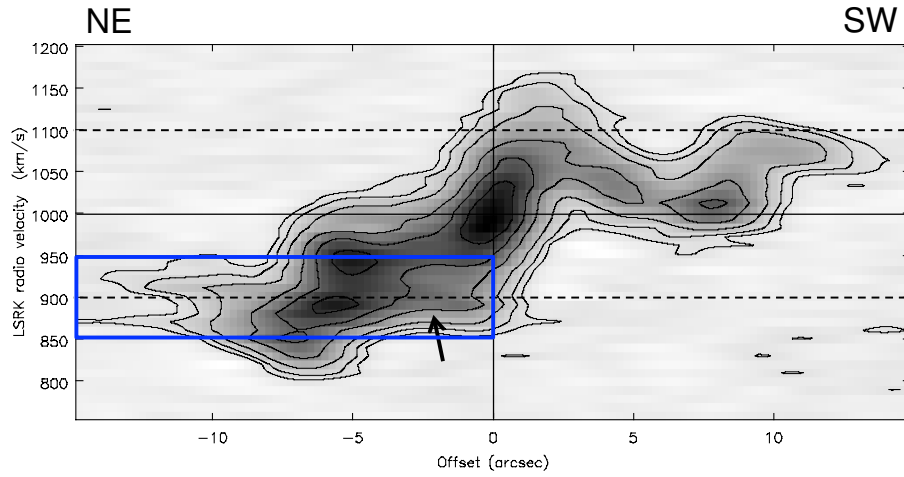


Fig. 32.— PVD of the slice shown in figure 31. The outflow component, centered near 900 km s^{-1} , is indicated with a black arrow. Note the double peak with separation 50 km s^{-1} near offset $Y = -5''$ and line splitting at $Y < -9''$. The contours are plotted at 0.05, 0.1, 0.2, 0.4, 0.6, 0.8 times the peak of $262 \text{ mJy beam}^{-1}$.

5.2. Mass and kinetic energy

Infrared and radio observations show that the nucleus is ongoing a starburst episode with a star formation rate of $SFR_{\text{core}} \sim (0.5-1) M_{\odot} \text{ yr}^{-1}$ (Krabbe et al. 1994; Kotilainen et al. 1996) (assuming that the energy output in the core is dominated by supernova explosions rather than AGN). As a consequence, the region is shocked by supernovae that generate non-thermal radiation and an ionization cone discussed above. Following Condon & Yin (1990), Krabbe et al. (1994) estimated the supernova rate in the nucleus using the 5-GHz continuum as $\mathcal{R}_{\text{SN}} = 0.024 \text{ yr}^{-1}$. The released energy during a starburst episode [$t_{\text{SB}} \gtrsim 1 \times 10^7 \text{ yr}$; Krabbe et al. (1994) and Kotilainen et al. (1996)] is then³

$$E_{\text{SN}} \sim \mathcal{R}_{\text{SN}} E_0 t_{\text{SB}} \sim 2 \times 10^{56} \text{ erg}, \quad (12)$$

where $E_0 = 10^{51} \text{ erg}$ is the energy released by a single type-II supernova explosion. It is of importance to compare this energy with the kinetic energy of the molecular gas outflow. Below, we consider the outflow mass estimates based on two limiting cases.

5.2.1. *Optically thick emission*

Inspecting the channel maps (e.g., figure 31), we find that the outflow contribution to the CO (1-0) flux is no more than about 10% in the central 1 kpc. If the mass of the molecular gas in the outflow is $M_{\text{out}} \sim 0.1 M_{\text{mol}} \sim 6 \times 10^7 M_{\odot}$, where M_{mol} is the total molecular gas mass in the central region ($r < 15''$; table 5), and $v_z = 180 \text{ km s}^{-1}$, the kinetic energy becomes $E_{\text{out}} \simeq M_{\text{out}} v_z^2 / 2 \sim 2 \times 10^{55} \text{ erg}$. This is an upper limit because the CO (1-0) emission is assumed optically thick (the conversion factor $X_{\text{CO}} = 0.8 \times 10^{20} \text{ cm}^{-2} (\text{K km s}^{-1})^{-1}$ was applied). Therefore, the derived energy released by supernova explosions is an order of magnitude higher than the upper limit of the molecular gas kinetic energy inferred from the measured CO (1-0) fluxes and velocities in the central region.

5.2.2. *Optically thin emission*

In the case of optically thin CO (1-0) emission, the total number of H_2 molecules can be calculated as

³Krabbe et al. (1994) estimated that the starburst has been going on for $\gtrsim 5 \times 10^7 \text{ yr}$. We adopt a lower limit based on the mass of the nuclear cluster estimated in section 4.1.

$$\mathcal{N}_{\text{H}_2} = f \frac{3k}{4\pi^3 \mu^2 \nu} \frac{1}{J+1} \exp \left[\frac{J(J+1)h\nu}{2kT_{\text{ex}}} \right] \left[1 - \exp \left(-\frac{(J+1)h\nu}{kT_{\text{ex}}} \right) \right]^{-1} I_{\text{CO}} A. \quad (13)$$

Here, $f \equiv [\text{H}_2]/[\text{CO}]$ is the abundance ratio of H_2 and CO molecules, h the Planck constant, k the Boltzmann constant, μ the dipole moment, J the rotational level in a transition $J+1 \rightarrow J$, ν the frequency of the line, T_{ex} the excitation temperature, $I_{\text{CO}} \equiv \int T_{\text{R}} dv$ the total integrated intensity (radiation temperature T_{R} integrated over velocity) of the CO line, and $A = \pi R^2$ the projected area (where R is the radius of the region). For a transition to the ground level, we have $J = 0$, $\mu = 0.11$ Debye, and $\nu = 115.271$ GHz, and equation 13 can be written as

$$\mathcal{N}_{\text{H}_2} = 2.31 \times 10^{14} f \left[1 - \exp \left(-\frac{5.53 \text{ K}}{T_{\text{ex}}} \right) \right]^{-1} \left(\frac{I_{\text{CO}}}{\text{K km s}^{-1}} \right) \left(\frac{A}{\text{cm}^2} \right). \quad (14)$$

We adopt an excitation temperature of $T_{\text{ex}} = 31$ K (Salak et al. 2014). The conversion between the brightness temperature and flux density is given by

$$\left(\frac{I_{\text{CO}}}{\text{K km s}^{-1}} \right) = 92.5 \left(\frac{\theta}{\text{arcsec}} \right)^{-2} \left(\frac{\nu}{115 \text{ GHz}} \right)^{-2} \left(\frac{\int S_{\text{CO}} dv}{\text{Jy km s}^{-1}} \right), \quad (15)$$

where θ is the diameter of the region. For the adopted CO (1-0) flux in the outflow in the central region $r < 15''$, we get $I_{\text{CO}} = 122.4 \text{ Jy km s}^{-1} = 12.6 \text{ K km s}^{-1}$. Assuming an abundance ratio of $f = 10^4$, the total mass within $r < R = 15''$ becomes $M_{\text{out}} = 1.41 \times 2m_{\text{H}} \mathcal{N}_{\text{H}_2} \sim 8 \times 10^6 M_{\odot}$, where m_{H} is the hydrogen atom mass and the factor 1.41 accounts for He and other elements. The kinetic energy of the nuclear outflow is then only $E_{\text{out}} \sim 10^{54}$ erg.

5.3. Dynamical evolution

The molecular gas outflow traced by CO (spur in figure 29) is evident up to a deprojected height of $z \sim 1$ kpc. Assuming spherical symmetry, the lower limit of the escape velocity at this radius from the center is given by $v_{\text{esc}} = \sqrt{2|\Phi|}$, where $\Phi = -GM/z$ is the gravitational potential (simplified as a point source). The total mass within this region is $M(z < 1 \text{ kpc}) \sim 1 \times 10^{10} M_{\odot}$, hence $v_{\text{esc}} \sim 300 \text{ km s}^{-1}$. The escape velocity is comparable but somewhat larger than the average outflow velocity, $v_{\text{out}} \lesssim v_{\text{esc}}$, indicating that the molecular gas outflow may be trapped in the potential well of the galaxy. Note that Phillips (1993) found a maximum outflow velocity of $\sim 380 \text{ km s}^{-1}$; the fastest gas clouds may be able to escape. For the

adopted distance of $z = 1$ kpc and velocity $v_{\text{out}} = 180 \text{ km s}^{-1}$, the dynamical age of the outflow is $t_{\text{out}} \sim z/v_{\text{out}} \sim 5 \times 10^6 \text{ yr}$, consistent with the estimate by Phillips (1993) based on NaI D spectra. This is shorter than the nuclear star-forming activity ($t_{\text{SB}} \gtrsim 1 \times 10^7 \text{ yr}$): the outflow is resupplied via supernova explosions during the starburst episodes.

If the masses and timescales are correct, the mass outflow rate from the central region of NGC 1808 is $\dot{M}_{\text{out}} \sim M_{\text{out}}/t_{\text{out}} \sim (1-10) M_{\odot} \text{ yr}^{-1}$, comparable to the total star formation rate in the starburst 500-pc region [$SFR \sim 5 M_{\odot} \text{ yr}^{-1}$ in all “hot spots” combined; (Krabbe et al. 1994)], yielding $\dot{M}_{\text{out}}/SFR \sim 0.2$ for the optically thin case. Note that, in spite of violent star formation feedback, evidenced by numerous supernova remnants and polar dust lanes, the nucleus and the $r < 500 \text{ pc}$ disk (including the ring) are very abundant in molecular gas. In order to replenish the gas reservoir, a mass inflow rate comparable to \dot{M}_{out} is required. This can be expected from the double bar and spiral arms. By comparison, the mass outflow rate in the nearby starburst galaxy NGC 253 is $\dot{M}_{\text{out}} \sim (3-9) M_{\odot} \text{ yr}^{-1}$ and the ratio $\dot{M}_{\text{out}}/SFR \sim 3$ (Bolatto et al. 2013a). Similarly, the ratio in M82 is $\dot{M}_{\text{out}}/SFR \sim 1$ (Walter et al. 2002; Salak et al. 2013): the quenching of star formation in NGC 1808 seems less efficient than in NGC 253 and M82.

It should be noted, however, that we cannot exclude the possibility that the outflow is too extended and diffuse to be sampled with the 12-m array without short-spacing correction, so the derivation of the outflow mass is largely uncertain. Combining 12-m array data with ACA (Atacama Compact Array) and total power data will clarify the spatial extent and energetics of the molecular gas outflow.

On the other hand, deep HST images of H α (e.g., figure 8) show little sign of extraplanar ionized gas in polar direction as far as the kpc-scale dust lanes. Could the dust lanes further out in the halo be associated with atom-dominated gas, traced with HI and possibly [C I] or [C II]? This question is related to the nature of superwinds in galaxies: what is their dominant ISM phase and what mechanisms govern phase transitions as the wind evolves?

6. Star formation and disk stability in the central 1 kpc

In section 3.1 we presented 2.8-mm continuum data that reveal the presence of circum-nuclear compact sources dominated by thermal emission. Note that the sources C1, C2, and C3 (figure 4 and table 4) are located along the nuclear spiral arm on the inside of the 500-pc ring detected in CO (1-0) (figure 33). Sources C1, C3, and C4 are spatially correlated with the mid-infrared sources denoted by M3, M2, M6-M8 and interpreted as young star clusters and HII regions embedded in dusty clouds (Galliano & Alloin 2008). The comparison of

the continuum and CO distributions (figure 33) also reveals that, apart from the SE region, there is no detected 2.8-mm continuum emission associated with the molecular 500-pc ring; star-forming activity and its feedback are more prominent in the inner $r < 400$ pc disk [see also, e.g., Saikia et al. (1990) for the distribution of supernova remnants that are also within the inner disk].

One of the long-standing problems in galactic dynamics is to understand the mechanism of transport of molecular gas from the nuclear ring near the inner Lindblad resonances, such as the 500-pc ring in NGC 1808, to the very center of the galaxy (< 1 pc). The main processes involved are nuclear bars and spiral arms. Both structures generate non-axisymmetric gravitational potential that exerts torque on the outer region (e.g., Schwarz 1984; Buta & Combes 1996; Combes et al. 2014). Angular momentum is transferred outward, while the material decays to lower orbits. In NGC 1808, the presence of a nuclear bar and a spiral arm is indicative of gas inflow from the 500-pc ring. In order to clarify its relation with star formation unveiled with radio continuum and infrared observations, we investigated the gravitational stability of the disk region between the CNB and the ring. The stability criterion can be expressed as a Q parameter for fluids (Safronov 1960; Toomre 1964),

$$Q_{\text{gas}} \equiv \frac{\alpha v_s \kappa}{\pi G \Sigma_{\text{gas}}}, \quad (16)$$

where α is a constant (assumed equal to unity here), v_s is the speed of sound related to the velocity dispersion of the ISM gas, σ_{mol} . The stability increases with velocity dispersion and epicyclic frequency κ (related to differential rotation), and decreases with gas surface density. When $Q_{\text{gas}} \lesssim 1$, the gaseous disk is unstable and likely to increase star forming activity. The resulting Q_{gas} , calculated with $v_s = \sigma_{\text{mol}}$, is shown in figure 34; the uncertainty of the derived values is high due to the variation in the CO-to-H₂ conversion factor X_{CO} , velocity dispersion, surface density, and rotation curve. Nevertheless, the result shows that the disk stability is somewhat low (although $Q_{\text{gas}} \gtrsim 1$) between 100 and 300 pc where the rotation curve exhibits a gentle slope, qualitatively consistent with the observational results above. The sudden drop beyond $r > 500$ pc (beyond the ring) should be taken with reserve as the signal-to-noise ratio is low in that region.

This result is different from the one found, e.g., in the Seyfert galaxy NGC 7469, where the instability is highest in the resonant ring ($Q_{\text{gas}} \lesssim 1$ and active star formation), while the gaseous disk is gradually more stable toward the galactic center (Fathi et al. 2015). The high Q_{gas} in the central 500 pc of NGC 1808 is comparable to the results obtained for a sample of nearby spiral galaxies including NGC 6946 (Romeo & Falstad 2013; Romeo & Fathi 2015). Contrary to the inner $r < 400$ pc disk, star formation activity in NGC 1808 appears less prominent outside the resonant 500-pc ring due to a high velocity gradient imposed by bar

dynamics (sections 3.3 and 4.2.2).

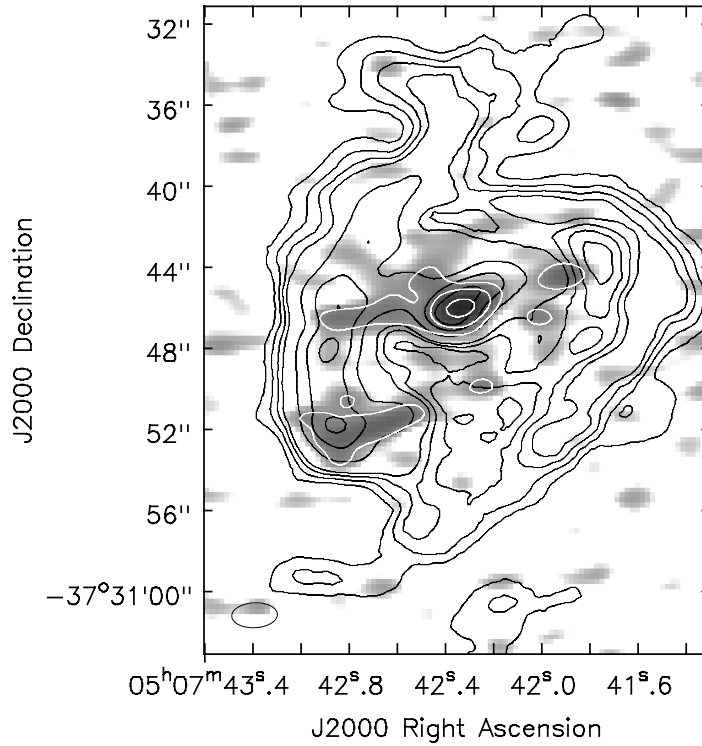


Fig. 33.— CO (1-0) integrated intensity contours (0.05, 0.1, 0.15, 0.2, 0.4, 0.6, 0.8 times the peak of $34 \text{ Jy beam}^{-1} \text{ km s}^{-1}$) superimposed on the 2.8-mm continuum image (grey scale and white contours at 0.1, 0.2, 0.4 times the peak of $2.6 \text{ mJy beam}^{-1}$).

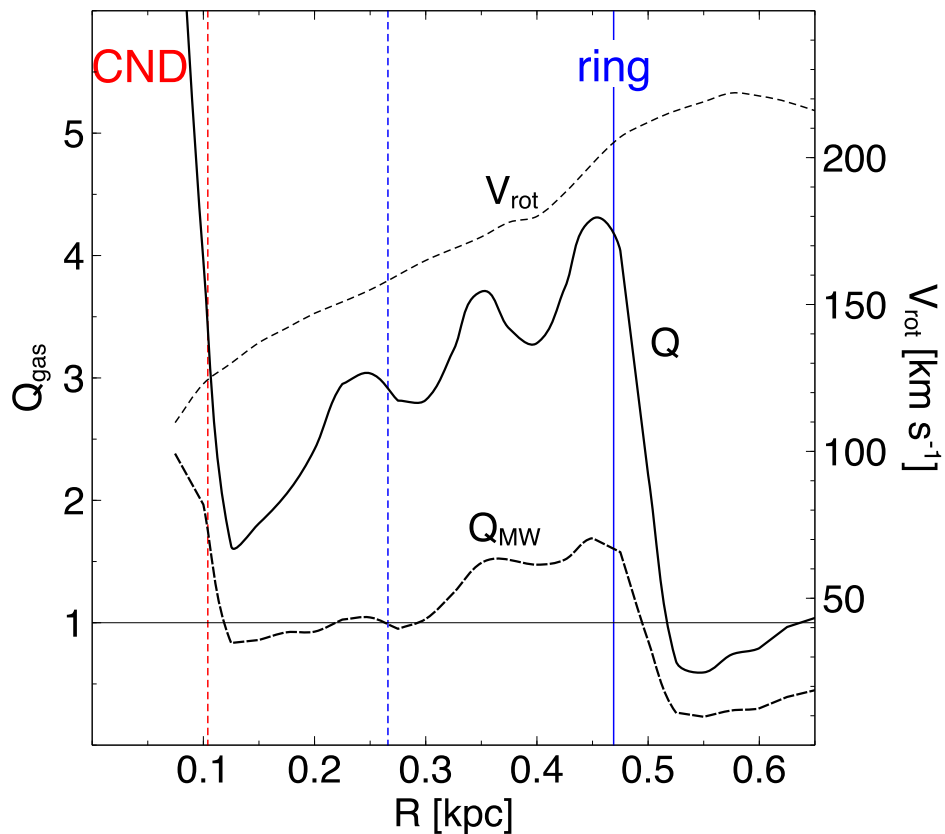


Fig. 34.— Stability parameter Q_{gas} for the gas disk in the central 0.6 kpc region derived by using two different CO-to-H₂ conversion factors: the Galactic value $X_{\text{MW}} = 2 \times 10^{20} \text{ cm}^{-2} (\text{K km s}^{-1})^{-1}$ and $X = X_{\text{MW}}/2.25$. The vertical lines mark the 500-pc ring (blue) and the CND (red). The dashed vertical lines are the standard deviations of the two regions (section 3.2.2).

7. Summary

We have presented the first high-resolution ALMA observations of CO (1-0) and 2.8 mm continuum in the barred starburst galaxy NGC 1808. Below is a summary of the main findings.

1. *Continuum emission.* Radio continuum at 2.8 mm (synthesized over four bands at 101, 103, 113, and 115 GHz) was detected at the nucleus and circumnuclear regions within $r < 400$ pc. The spectral index (α) image confirms that the nucleus is dominated by non-thermal (synchrotron) emission with $\alpha \simeq -1$.
2. *Molecular gas distribution.* High-resolution CO (1-0) images revealed four distinct components of molecular gas: (1) compact circumnuclear disk (CND) within $r < 200$ pc, (2) 500-pc ring, (3) gas-rich galactic bar with semi-major axis $a_b \simeq 3$ kpc, and (4) global (kpc-scale) and nuclear ($r < 400$ pc) spiral structure. In the inner $r < 400$ pc disk, molecular gas is distributed in a spiral pattern.
3. *Molecular gas kinematics.* Basic geometric and kinematic parameters (position angle, inclination, rotation curve, and velocity dispersion) were derived for the central 1 kpc region using the ^{3D}Barolo code. Two systemic velocities were found (998 km s⁻¹ for the CND and 964 km s⁻¹ for the 500-pc ring), indicating a kinematic offset. Streaming motion with magnitude ~ 50 km s⁻¹ is revealed on the inner side of a nuclear spiral arm. On a large scale, molecular gas clouds exhibit conspicuous non-circular motions dominated by the primary bar, with a velocity gradient (shear) of $v_{\text{sh}} \simeq (0.2-1)$ km s⁻¹ pc⁻¹ across the molecular gas ridges on the leading side of the bar.
4. *Rotation curve decomposition and dynamical mass.* The rotation curve derived from the CO (1-0) emission was deconvolved into a stellar bulge (mass $M_{\text{B1}} \sim 1.25 \times 10^{10} M_{\odot}$), a major core that comprises a nuclear bar and molecular medium ($M_{\text{B2}} \sim 7.2 \times 10^8 M_{\odot}$), and an unresolved minor core, possibly a nuclear star cluster or black hole with mass $M_{\text{core}} \sim 1 \times 10^7 M_{\odot}$ surrounded by an embedded molecular gas disk with a radius $r < 50$ pc.
5. *Bar dynamics and orbital resonances.* The bar pattern speed of the large-scale bar was derived as $\Omega_b = 56 \pm 11$ km s⁻¹ kpc⁻¹ from the position-velocity diagram assuming a cloud-orbit model. For a flat rotation curve of 190 km s⁻¹ at $r > 1.5$ kpc, the pattern speed yields a corotation radius of $r_{\text{CR}} \simeq 3.4$ kpc and the ratio $r_{\text{CR}}/a_b \simeq 1.1$, consistent with theoretical predictions for weak bars. An inner Lindblad resonance is located at ~ 500 pc, coincident with the location of the molecular gas ring.

6. *Molecular gas outflow.* We presented evidence of a molecular gas outflow from the nuclear starburst region ($r < 250$ pc). The outflow has a maximum velocity of $v_{\text{out}} \sim 180$ km s⁻¹ and a total kinetic energy two orders of magnitude smaller than the energy released by supernova explosions in the nucleus.
7. *Gas disk stability and star formation.* In the region 200 pc $< r < 400$ pc, the stability parameter of the gas disk, Q_{gas} , is lower than average, allowing enhanced star formation activity, consistent with observations of circumnuclear “hot spots”.

The authors thank an anonymous referee for careful reading and many useful suggestions. We thank the graduate students Y. Yamada, S. Hisamatsu, and I. Tanaka for assistance during the observations with ASTE, and professor M. Seta for support in data reduction. D.S. is grateful to S. Imai for heartwarming discussions and to E. Galliano for providing the VLT K_s image. This paper makes use of the following ALMA data: ADS/JAO.ALMA#2012.1.01004.S. ALMA is a partnership of ESO (representing its member states), NSF (USA) and NINS (Japan), together with NRC (Canada) and NSC and ASIAA (Taiwan), in cooperation with the Republic of Chile. The Joint ALMA Observatory is operated by ESO, AUI/NRAO and NAOJ. Based on observations made with the NASA/ESA Hubble Space Telescope, and obtained from the Hubble Legacy Archive, which is a collaboration between the Space Telescope Science Institute (STScI/NASA), the Space Telescope European Coordinating Facility (ST-ECF/ESA) and the Canadian Astronomy Data Centre (CADM/NRC/CSA). This research has made use of the NASA/IPAC Extragalactic Database (NED) which is operated by the Jet Propulsion Laboratory, California Institute of Technology, under contract with the National Aeronautics and Space Administration.

A. HCN (4-3) observations with ASTE

Single-dish observations with Atacama Submillimeter Telescope Experiment (ASTE)⁴ were conducted in 2014 September and October with single pointing toward the galactic center (table 8). The frontend receiver CATS 345 was tuned to the HCN ($J = 4 \rightarrow 3$) line at the rest frequency of 354.505473 GHz in the upper side band. The signal was down-converted to an intermediate frequency and resolved with an XF-type autocorrelation spectrometer with a total bandwidth of 512 MHz (443 km s⁻¹) and fine spectral resolution of 0.5 MHz.

⁴The ASTE telescope is operated by National Astronomical Observatory of Japan (NAOJ).

The bandwidth was wide enough to cover the velocity range of the HI and CO (3-2) lines (Koribalski et al. 1993; Salak et al. 2014), hence we assumed that the HCN (4-3) line does not exhibit a wider profile. Intensity calibration was performed by the standard chopper wheel method that yielded the antenna temperature T_A^* corrected for atmospheric and ohmic losses (Ulich & Haas 1976). Each time the receiver was tuned, an intensity calibrator (Orion KL) was observed to measure a reference spectrum at the same frequency. An appropriate scaling factor was then applied to correct for intensity fluctuations and to convert T_A^* to the main beam temperature, $T_{\text{mb}} \equiv T_A^*/\eta_{\text{mb}}$, where η_{mb} is the main beam efficiency. The derived scaling factor of 1.6 yielded $\eta_{\text{mb}} \simeq 0.6$, consistent with the telescope data provided online. Telescope pointing was checked after every observing run of about one hour and the relative offset was typically $< 3''$.

Data reduction was done by using the NEWSTAR tool developed by Nobeyama Radio Observatory of the National Astronomical Observatory of Japan. Raw data were converted to spectra, flagged, baseline-subtracted (first-order polynomial), and smoothed to a velocity resolution of 5.5 km s^{-1} . The basic properties of the line are given in table 8. The uncertainty of the integrated intensity is estimated by $\Delta I = \sqrt{\Delta I_{\text{rms}}^2 + \Delta I_{\text{b}}^2}$, where $\Delta I_{\text{rms}} = \Delta T_{\text{rms}} \sqrt{\Delta v_{\text{ch}} v_{\text{int}}} = 0.10 \text{ K km s}^{-1}$ is due to the r.m.s. noise and $\Delta I_{\text{b}} = \Delta T_{\text{rms}} \Delta v_{\text{int}} \sqrt{\Delta v_{\text{ch}} / \Delta v_{\text{b}}} = 0.18 \text{ K km s}^{-1}$ is the contribution from the baseline fitting. Here, $\Delta v_{\text{int}} = 320 \text{ km s}^{-1}$ is the velocity width of the integrated spectrum, $\Delta v_{\text{ch}} = 5.5 \text{ km s}^{-1}$ the channel width, and $\Delta v_{\text{b}} = 80 \text{ km s}^{-1}$ the total range of the baseline fitting.

A.1. HCN (4-3) emission in the galactic nucleus

In figure 35 we show the spectrum of HCN (4-3) toward the galactic center at $(\alpha, \delta)_{\text{J2000.0}} = (5^{\text{h}}7^{\text{m}}42^{\text{s}}.06, -37^{\circ}30'44''.42)$ measured using ASTE whose beam size was FWHM = $22''$ (1.1 kpc). The profile is notably different from the triple peak seen in CO (1-0) [as well as in CO (3-2) and ^{13}CO (3-2); Salak et al. (2014)] in the inner 1 kpc and much more similar to the CO profile within the central $r < 250 \text{ pc}$ (figure 17). The velocity of 998 km s^{-1} at the emission peak calculated with Gaussian fitting (table 9) also resembles the one derived from CO at the center. This result is not surprising if HCN (4-3) emission originates almost entirely in the CNB and much less in the 500-pc ring. Given the expected effective critical density⁵ of the order of $n_{\text{cr}} > 10^4 \text{ cm}^{-3}$ for HCN (4-3) at any temperature between 10 and a few hundred K (e.g., Shirley 2015), the line is known to trace extremely dense molecular

⁵The critical density is defined as the ratio of the Einstein coefficient for spontaneous decay between an upper and a lower energy level (u and l), A_{ul} , and the collisional cross section σ . The effective critical density includes the effects of radiative trapping described by the photon escape probability β , and can be defined

medium commonly observed in galactic nuclei.

as $n_{\text{cr}} \equiv \beta A_{\text{ul}}/\sigma$.

Table 8: Observational summary.

ASTE 10 m	
Observation date	2014 Sep. 16-17, Oct. 1-2
Intensity calibrator	Orion KL
Pointing calibrator	R Dor
Receiver	CATS 345
Spectrometer bandwidth	512 MHz (445 km s ⁻¹)
Velocity resolution ^a	0.42 km s ⁻¹
Beam FWHM	22'' (1.1 kpc)
Integration time	2.6 hr
1 σ sensitivity in T_{mb}	2.5 mK

^aSmoothed to 5.5 km s⁻¹.

Table 9: HCN (4-3) line parameters (Gaussian fit).

Parameter	This work	Zhang et al. (2014)
Peak T_{mb} [mK]	15.2 \pm 2.8	
Line FWHM [km s ⁻¹]	144.2 \pm 8.7	
Peak velocity [km s ⁻¹]	998.6 \pm 3.3	
Integrated intensity [K km s ⁻¹]	2.3 \pm 0.2	2.5 \pm 0.2

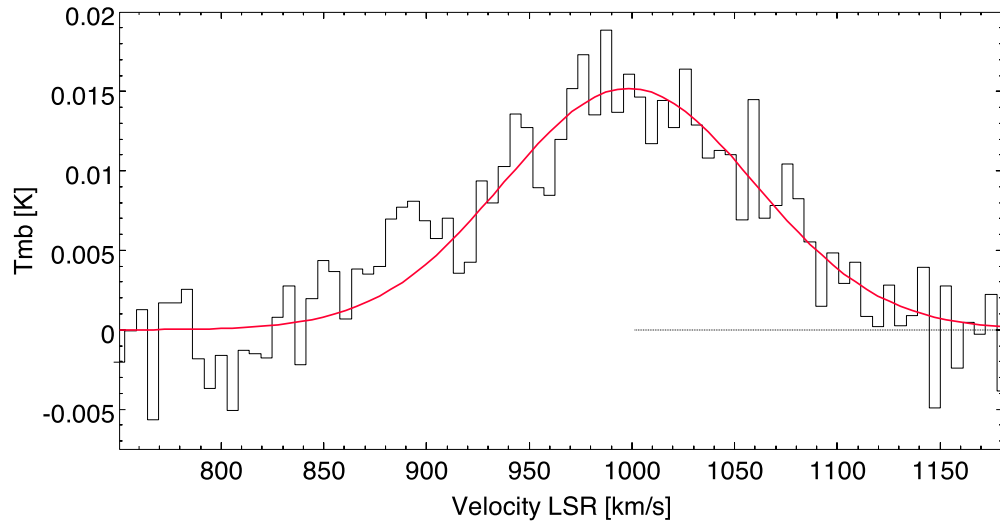


Fig. 35.— HCN (4-3) spectrum toward the galactic center.

REFERENCES

- Aalto, S., Booth, R. S., Black, J. H., Koribalski, B., & Wielebinski, R. 1994, *A&A*, 286, 365
- Aalto, S., Hüttemeister, S., Scoville, N. Z., & Thaddeus, P. 1999, *ApJ*, 522, 165
- Athanassoula, E. 1992, *MNRAS*, 259, 328
- Athanassoula, E. 1992, *MNRAS*, 259, 345
- Awaki, H., Ueno, S., Koyama, K., Tsuru, T., & Iwasawa, K. 1996, *PASJ*, 48, 409
- Binney, J., Gerhard, O. E., Stark, A. A., Bally, J., & Uchida, K. I. 1991, *MNRAS*, 252, 210
- Binney, J., & Tremaine, S. 2008, *Galactic Dynamics*, 2nd ed. (New Jersey: Princeton University Press), 528-539
- Bolatto, A., Warren, S. R., Leroy, A. K., et al. 2013, *Nature*, 499, 450
- Bolatto, A., Wolfire, M., and Leroy, A. K. 2013, *ARA&A*, 51, 207
- Burbidge, E. M. & Burbidge, G. R. 1968, *ApJ*, 151, 99
- Buta, R., & Combes, F. 1996, *Fund. Cosm. Phys.*, 17, 95
- Chevalier, R. A. & Clegg, A. W. 1985, *Nature*, 317, 44
- Collison, P. M., Saikia, D. J., Pedlar, A., Axon, D. J., and Unger, S. W. 1994, *MNRAS*, 268, 203
- Combes, F., García-Burillo, S., Casasola, V., et al. 2013, *A&A*, 558, A124
- Combes, F., García-Burillo, S., Casasola, V., et al. 2014, *A&A*, 565, A97
- Condon, J. J. 1987, *ApJS*, 65, 485
- Condon, J. J., & Yin, Q. F. 1990, *ApJ*, 357, 97
- Condon, J. J. 1992, *ARA&A*, 30, 575
- Contopoulos, G. 1980, *A&A*, 81, 198
- Dahlem, M., Aalto, S., Klein, U., et al. 1990, *A&A*, 240, 237
- Davis, T. A., Bureau, M., Cappellari, M., Sarzi, M., & Blitz, L. 2013, *Nature*, 494, 328
- Debattista, V. P. & Shen, J. 2007, *ApJ*, 654, L127

- de Vaucouleurs, G. de Vaucouleurs, A., Corwin, JR., H. G., et al. 1991, Third Reference Catalogue of Bright Galaxies, ver. 3.9
- Di Teodoro, E. M. & Fraternali, F. 2015, MNRAS, 451, 3021
- Downes, D., Reynaud, D., Solomon, P. M., & Radford, S. J. E. 1996, ApJ, 461, 186
- Fathi, K., Izumi, T., Romeo, A. B., et al. 2015, ApJ, 806, L34
- Forbes, D. A., Boisson, C., & Ward, M. J. 1992, MNRAS, 259, 293
- Fujimoto, Y., Tasker, E. J., Wakayama, M., & Habe, A. 2014, MNRAS, 439, 936
- Galliano, E., Alloin, D., Pantin, E., Lagage, P. O., and Marco, O. 2005, A&A, 438, 803
- Galliano, E. & Alloin, D. 2008, A&A, 487, 519
- García-Burillo, S., Combes, F., Schinnerer, E., Boone, F., & Hunt, L. K. 2005, A&A, 441, 1011
- García-Burillo, S., Combes, F., Usero, A., et al. 2014, A&A, 567, A125
- García-Lorenzo, B., Mediavilla, E., Arribas, S., & del Burgo, C. 1997, ApJ, 483, L99
- Gillessen, S., Eisenhauer, F., Trippe, S., et al. 2009, ApJ, 692, 1075
- Heike, K. & Awaki, H. 2007, PASJ, 59, 531
- Heller, C. H., Shlosman, I., & Athanassoula, E. 2007, ApJ, 657, L65
- Hirota, A., Kuno, N., Baba, J., et al. 2014, PASJ, 66, 46
- Jarrett, T. H., Chester, T., Cutri, R., Schneider, S. E., & Huchra, J. P. 2003, AJ, 125, 525
- Jiménez-Bailón, E., Santos-Lleó, M., Dahlem, M., et al. 2005, A&A, 442, 861
- Kennicutt, R. C., Jr. 1998, ARA&A, 36, 189
- Koda, J., Sofue, Y., Kohno, K., et al. 2002, ApJ, 573, 105
- Koda, J. & Sofue, Y. 2006, PASJ, 58, 299
- Koribalski, B., Dahlem, M., Mebold, U., & Brinks, E. 1993, A&A, 268, 14
- Koribalski, B., Dettmar, R.-J., Mebold, U., & Wielebinski, R. 1996, A&A, 315, 71
- Kormendy, J. & Ho, L. C. 2013, ARA&A, 51, 511

- Kotilainen, J. K., Forbes, D. A., Moorwood, A. F. M., van der Werf, P. P., & Ward, M.J. 1996, *A&A*, 313, 771
- Krabbe, A., Sternberg, A., & Genzel, R. 1994, *ApJ*, 425, 72
- Krips, M., Martín, S., Eckart, A., et al. 2011, *ApJ*, 736, 37
- Kuno, N., Nakai, N., Sorai, K., Vila-Vilaró, B., & Handa, T. 2000, *PASJ*, 52, 775
- Lauberts, A. & Valentijn, E. A., *The Surface Photometry Catalogue of the ESO-Uppsala Galaxies*, ESO, Garching
- Leroy, A., Walter, F., Martini, P. et al. 2015, *ApJ*, 814, 83
- Lindblad, P. O., & Lindblad, P. A. B. 1994, *ASPC*, 66, 29L
- Maciejewski, W. & Small, E. E. 2010, *ApJ*, 719, 622
- McCormick, A., Veilleux, S., & Rupke, D. S. N. 2013, *ApJ*, 774, 126
- McMullin, J. P., Waters, B., Schiebel, D., Young, W., & Golap, K. 2007, *Astronomical Data Analysis Software and Systems XVI (ASP Conf. Ser. 376)*, ed. R. A. Shaw, F. Hill, & D. J. Bell (San Francisco, CA: ASP), 127
- Meidt, S. E., Schinnerer, E., García-Burillo, S., et al. 2013, *ApJ*, 779, 45
- Meurer, G., Ferguson, H., et al. 2002, SINGG collaboration
- Morgan, W. W. 1958, *PASP*, 70, 415
- Murray, N., Quataert, E., & Thompson, T. A. 2005, *ApJ*, 618, 569
- Murray, N., Ménard, B., & Thompson, T. A. 2011, *ApJ*, 735, 66
- Nakai, N., Hayashi, M., Handa, T., Sofue, Y., & Hasegawa, T. 1987, *PASJ*, 39, 685
- Nath, B. B. & Silk, J. 2009, *MNRAS*, 396, L90
- Oliva, E., Origlia, L., Kotilainen, J. K., & Moorwood, A. F. M. 1995, *A&A*, 301, 55
- Onishi, K., Iguchi, S., Sheth, K. & Kohno, K. 2015, *ApJ*, 806, 39
- Pérez-Ramírez, D., Knapen, J. H., Peletier, R. F., et al. *MNRAS*, 317, 234
- Phillips, A. C. 1993, *AJ*, 105, 486

- Plummer, H. C. 1911, MNRAS, 71, 460
- Reif, K., Mebold, U., Goss, W. M., van Woerden, & H., Siegman, B., 1982, A&AS, 50, 451
- Rogstad, D. H., Lockhart, I. A., & Wright, M. C. H. 1974, ApJ, 193, 309
- Romeo, A. B. & Falstad, N. 2013, MNRAS, 433, 1389
- Romeo, A. B. & Fathi, K. 2015, MNRAS, 451, 3107
- Safronov, V. S. 1960, AnAp, 23, 979
- Saikia, D. J., Unger, S. W., Pedlar, A., et al. 1990, MNRAS, 245, 397
- Sakamoto, K., Okumura, S. K., Ishizuki, S., & Scoville, N. Z. 1999, ApJS, 124, 403
- Sakamoto, K., Baker, A. J., & Scoville, N. Z. 2000, ApJ, 533, 149
- Sakamoto, K., Aalto, S., Combes, F., Evans, A., & Peck, A. 2014, ApJ, 797, 90
- Salak, D., Nakai, N., Miyamoto, Y., Yamaguchi, A., & Tsuru, T. G. 2013, PASJ, 66, 65
- Salak, D., Nakai, N., & Kitamoto, S. 2014, PASJ, 66, 96
- Shirley, Y. L. 2015, PASP, 127, 299
- Schiano, A. V. R. 1985, ApJ, 299, 24
- Schwarz, M. P. 1984, MNRAS, 209, 93
- Sérsic, J. L. & Pastoriza, M. 1965, PASP, 77, 287
- Sharp, R. G., & Bland-Hawthorn, J. 2010, ApJ, 711, 818
- Sheth, K., Regan, M. W., Vogel, S. N., & Teuben, P. J. 2000, ApJ, 532, 221
- Sofue, Y., Tutui, Y., Homma, M., et al. 1999, ApJ, 523, 136
- Sofue, Y., & Rubin, V. 2001, ARA&A, 39, 137
- Sofue, Y. 2013, PASJ, 65, 118
- Tacconi-Garman, L. E., Sternberg, A., & Eckart, A. 1996, AJ, 112, 918
- Tacconi-Garman, L. E., Sturm, E., Lehnert, M., Lutz, D., Davies, R. I., and Moorwood, A. F. M. 2005, A&A, 432, 91

- Terashima, Y., Iyomoto, N., Ho, L. C., & Ptak, A. F. 2002, *ApJS*, 139, 1
- Toomre, A. 1964, *ApJ*, 139, 1217
- Tully, R. B. 1988, *Nearby Galaxy Catalog*
- Ulich, B. L., & Haas, R. W. 1976, *ApJS*, 30, 247
- Véron-Cetty, M.-P. & Véron, P. 1985, *A&A*, 145, 425
- Wada, K. 1994, *PASJ*, 46, 165
- Walcher, C. J., van der Marel, R. P., McLaughlin, D., et al. 2005, *ApJ*, 618, 237
- Walter, F., Weiss, A., & Scoville, N. 2002, *ApJ*, 580, L21
- Veilleux, S., Cecil, G., & Bland-Hawthorn, J. 2005, *ARA&A*, 43, 769
- Young, J. S. & Scoville, N. Z. 1991, *ARA&A*, 29, 581
- Zhang, Z.-Y., Gao, Y., Henkel, C., Zhao, Y., Wang, J., et al. 2014, *ApJ*, 784, L31